Research Papers

Novel laurel aromatic evergreen biomass derived hierarchical porous carbon nanosheet as sustainable electrode for high performance symmetric supercapacitor

Erman Taer [a], Apriwandi [a], Windasari [a], Rika Taslim [b,*], Mohamad Deraman [c]

[a] *Department of Physics, Faculty of Mathematic and Natural Sciences, University of Riau, Simpang Baru, Pekanbaru 28293, Indonesia*
[b] *Department of Industrial Engineering, Faculty of Science and Technology, Islamic State University of Sultan Syarif Kasim, Pekanbaru 28293, Indonesia*
[c] *School of Applied Physics, Faculty of Science and Technology, Universiti Kebangsaan Malaysia, 43600 Bangi, Selangor, Malaysia*

ABSTRACT

Biomass-based activated carbon with features combinations of 2D nano-structure, 3D hierarchical porous, and self−/co-doping active heteroatoms have proven excellent performance as sustainable electrodes for high-energy supercapacitors. Therefore, this study aims to obtain activated carbon with 2D nanosheet, 3D hierarchical pores, and self-oxygen doped from the typical aromatic biomass of Indonesian laurel aromatic evergreen (ILAE), *Laurus nobilis*. It was carried out using a fast and toxic residue-free strategy as an active material for symmetrical supercapacitors. The optimization of the activated carbon structure was controlled through the activating agent ratio in high-temperature pyrolysis. It was discovered that the prepared ILAE carbon material has a 2D gauze-like nanosheet structure with a hierarchical pore network that enables fast and efficient accessibility. Furthermore, the porosity of the optimal ILAE-activated carbon possessed enriched micropores of 88 % and confirmed mesopores of 12 % with a high carbon content of 95.07 % and 4.49 % functional oxygen as self-doping heteroatom. In two-electrode configuration systems, the ILAE nanosheet-activated carbon-based supercapacitor exhibits excellent electrochemical performance with a high specific capacitance of 205 F g^{-1} at 1 A g^{-1} in a 1 M H$_2$SO$_4$ electrolyte. Furthermore, their capability rate was maintained at 81.16 % in 10 A g^{-1} with an optimum coulombic efficiency of 81.66 %. Moreover, the symmetrical supercapacitor device in aqueous electrolyte performed excellent energy output behaviors as high as 21.56 Wh kg^{-1} with maximum power output of 1.101 kW kg^{-1}, respectively. This indicated that the novel ILAE biomass proves high potential as a source of activated carbon enrich-nanosheet with 3D hierarchical pores prepared with the up-to-date approach to enhance the performance of electrochemical energy storage devices.

1. Introduction

The exploitation of coal, oil, and natural gas as conventional energy sources for decades has caused serious problems on the planet, especially environmental issues, global warming, climate change, and air-water-soil pollution [1,2]. Other factors such as illegal logging, the reduction of the "world's lungs", the narrowing of reforestation land, industrial residues, electronic and chemical wastes also contribute to the environmental issues for human survival [3,4]. This makes it necessary to search for renewable energy sources, with efficient conversion systems, and effective storage devices to achieve promising solutions for environmental sustainability [5,6]. Although the use of multi-generation solar cell technology, windmills, and water dam have

potential for clean energy sources and sustainable green energy conversion systems, periodic availability still hinders their continuous application [7–9]. Energy storage devices are expected to come with their best performance to support the renewable energy conversion system [10,11]. Currently, the battery is one of the most widely consumed commercial energy storage devices that can store electrical energy through typical chemical reactions [12]. However, the battery failed to harvest the energy generated from renewable energy sources due to unexpected power fluctuations. The use of batteries for larger electrical equipment can also reduce power density, thereby hindering their application at more complex scales. Previous investigations have established that supercapacitors are the best candidates for electrochemical energy storage devices [13]. This is because of their

extraordinary power density, which is larger than batteries, near-infinite cycle life, high conductivity, good stability, and the process of charging/discharging is repeatable, fast, and safe [14,15]. This makes supercapacitors applicable to a wide range of applications from simple circuits to complex sweetened electrical equipment such as LED circuits, electric motors, crane systems, pulse laser components, and telecommunications [16,17]. Moreover, relatively low specific energies of supercapacitors also need to be increased without reducing the high power density.

Generally, an active material is required to obtain high electrochemical performance in supercapacitor devices. Based on previous reports [18–20], the electrode active material consists of metal oxides/transitions, conduction polymers, and carbon. Referring to the pseudocapacitor type, the electrode materials derived from transition metal oxides have several advantages [21]. These include high energy density achieving the performance of traditional batteries and faradaic redox reaction which combines the properties of pseudocapacitance and electrochemical double layer capacitor (EDLC). The conductive polymeric material also confirms the good mechanical properties of potential flexible devices [20,22]. This outstanding performance has led to high-level applications of supercapacitors in military and aerospace technology. However, the commercialization of the electrode base material depends on the electrochemical performance and the consideration of source availability, cost, and environmental protection. Metal oxide resources are considered scarce, expensive, and allow potential environmental pollution on large exploitation, making it difficult to achieve large-scale applications. Meanwhile, the conducting polymeric materials of chemically engineered fossil products for pseudocapacitors are limited by poor stability and lower conductivity during redox reactions followed by toxic residues. The formation of electric double-layer capacitors in the supercapacitors also reduces conductive properties.

Currently, activated carbons have been widely used in commercial capacitors due to their low cost, good chemical stability, infinite cycle life, and extraordinarily stable EDLC properties. Biomass-based activated carbon with abundant renewable energy sources and low cost has also gained much attention. According to a previous report, waste biomass was proposed as a porous carbon precursor for electrodes in supercapacitors with enhanced performance. It was also discovered that various strategies and the extraction of the potential of biomass carbon lead to high electrical conductivity, unique 2D—3D morphologies such as nanosheets, nanofibers, 3D hierarchical pores, and the addition of active hetero-atoms such as N, O, and S representing its exceptional storage. The precursor biomass was reported to have tremendous potential as a porous carbon source with various material features favorable for enhanced supercapacitor performance such as oak nutshell [23], eucalyptus-bark [24], alfalfa flowers [25], cornstalk pith [26], *Typha orientalis* leaves [27], watermelon peel [28], and native European deciduous trees [29].

Recently, porous carbon with its unique combination of 2D nano-coupled behavior, 3D hierarchical pores, and the addition of active hetero-atom doping has shown significant potential to increase the energy density of supercapacitors [30–32]. It was discovered that 2D nanostructures such as nanofiber-nanosheets allow active materials to have unique electric charge transport features endowed by nanoscale thickness, infinite length, and well-defined 2D layered structures [33]. This behavior is closely related to the ability to maintain high EDLC power in complex electronic device applications. Furthermore, 3D hierarchical pore morphology plays an important role in providing highly active sites and relatively barrier-free ion migration pathways in all directions. The well-defined pore control significantly controls the synchrony of the energy boost without reducing the power density of the device [34]. The addition of self/co-doping active heteroatoms allows the EDLC device to have a high wettability feature leading to a pseudocapacitance effect on the electrode material [35].

According to Yang et al. 2020, natural rattan (*Plectocomia himalayan Griff.*) was converted as porous carbon by a combination of nanosheet

morphology and rich miro-mesopores with a specific surface area of 2436 $m^2 g^{-1}$ [36]. The results showed that the activated carbon shows a capacitive performance of 221 F g^{-1} at 0.5 A g^{-1}. A similar combination of carbon nanosheets and 3D hierarchical pores was studied by Selvaraj et al. (2021) from the *Prosopis juliflora* wood resource [31]. The outstanding electrochemical performance of the supercapacitor was demonstrated at a specific capacitance of 588 F g^{-1}, which match the transition metal oxide active materials and conducting polymers with an energy density of 32.9 Wh kg^{-1}, corresponding to the performance of commercial batteries. Recent studies with similar high-performance porous nanosheet-hierarchical features were also obtained from pecan shell precursors [37] and lemongrass [38]. The combination of 3D hierarchical pores and co-doping rich in N, O, P of peach gum-based carbon also increased the energy density significantly by 76.87 Wh kg^{-1} with excellent cycle, ultrahigh specific capacitance, and good stability [39]. However, the outstanding features of the combination coupled with the enhanced electrochemical performance produced still have some disadvantages, especially the approaches and strategies that have been used. Most of the above studies selected the template method, el-spin, a typical metal oxide mixture that has a high complexity, time-consuming procedure, and non-safety which tends to produce a brittle, corrosive, as well as toxic morphological framework. The features of the complex combination are very difficult to find in biomass precursors.

The biomass of *Laurus nobilis*, popularly known as Laurel Aromatic Evergreen (ILAE) or bay leaf, is one of popular herbs that have a distinctive aroma. The plant is usually used as a flavoring powder and is classified as a flavoring spice in food. It is found in mountainous areas of the Mediterranean, southern Turkey, northern Syria, southern Spain, north-central Portugal, northern Morocco, and the Canary Islands. Moreover, the plant is growing quite rapidly in Indonesia because of the consumption of seasonings that add a delicious aroma to food. The characteristic volatile that evokes certain aromas is also assumed to have extraordinary potential in their morphological structure of carbon. In detail, the volatile compounds contained in *Laurus nobilis* leaves are dominated by 1,8-cineole, followed by sabinene, α-terpinyl acetate, linalool, eugenol, methyl eugenol, and α-pinene [40]. Furthermore, their organic-nonorganic components are composed of cellulose, hemicellulose, and lignin which are enriched by K, Ca, and Mg [41,42]. However, there is no information on its leaf waste as a carbon source for electrochemical energy storage applications.

This study reports a safe, cost-effective, and rapid strategy to obtain porous carbon with a 3D hierarchical structure and nanosheets based on the typical aromatic biomass of *Laurus nobilis* for supercapacitor applications. Typical aromatic biomass precursors are converted to porous carbon through chemical-physical activation. The optimization of the morphological structure was controlled through the ratio of activating agents at 1:0.3, 1:0.5, and 1:0.7. Subsequently, the degradation of impurity compounds was carried out through integrated one-stage pyrolysis in an N_2 and CO_2 gas environment. The porous carbon displays a unique combination of 2D nanosheet structures, 3D hierarchical pores, and oxygen self-doping active heteroatoms that enhance the high performance of the electrode material. Using symmetric supercapacitor cells, the best electrode produces a specific capacitance of 205 F g^{-1} at 1 mVs^{-1} with a capability rate of 81.16 % at 10 mVs^{-1}. These results indicate that the 2D nanosheet structure associated with rich micropores and hierarchically linked 3D mesopores significantly contributes to the improvement of the ultra-fast and excellent ion adsorption/desorption capability at the 0.5-ILAE-SPC symmetrical electrode.

2. Materials and methods

2.1. Preparation of Laurus nobilis leaves precursor powder

Laurus nobilis leaves, Indonesian Laurel Aromatic Evergreen (ILAE) were obtained from a spice plantation in Duri city, Riau province. The parts of the *Laurus nobilis plant* are focused on their dried leaf waste
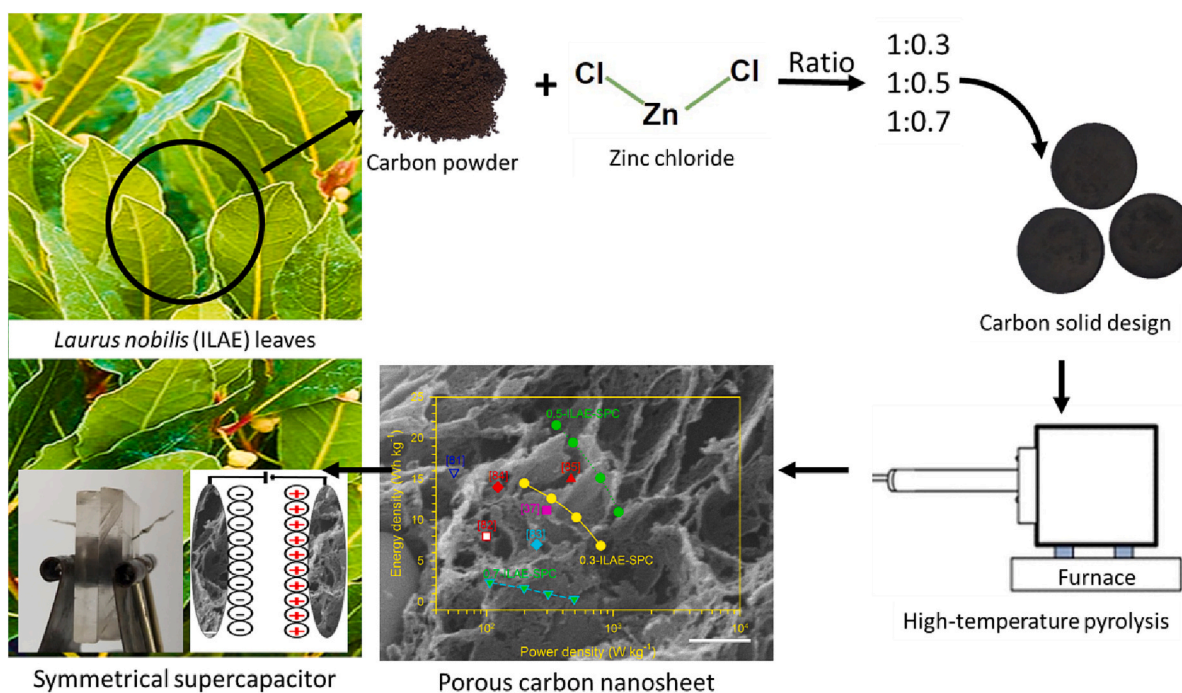
Scheme 1. Preparation of porous carbon nanosheet derived *Laurus nobilis* (ILAE) biomass

which is not used for any purpose. The leaves' precursors were separated from the branches, washed using distilled water, and dried in the sunlight for 12 h. Subsequently, the precursor was crushed, cut into small pieces the size of about 2×1 cm, and dried using an oven at 110 °C for 48 h. The dried samples were pre-carbonized at a low temperature of 250 °C under a vacuum system. The leaves are finely ground using a mortar to obtain powders precursor and continued with ball miller to possess smaller particle sizes. The homogenated particle size was performed by sifting the precursor with a 250 mesh sieve, where a total of 120 g was collected in particle sizes <60 μm.

2.2. Preparation of porous carbon from Laurus nobilis leaves

The homogenated *Laurus nobilis* leaves powder was chemically activated by mixing the precursor with the $ZnCl_2$ activating agent at different solution concentrations. The mass ratio of precursor powder/ $ZnCl_2$ is 1:0.3, 1:0.5, and 1:0.7. Meanwhile, the concentration ratio of the $ZnCl_2$ solution applied is relatively different from most previous reports. This is because the experiment was carried out to maintain the self-adhesiveness of the precursors and obtain carbons that can design bond-free solid electrodes for their absolute conductivity, as stated in the proposed novelty. The mixture of precursor powder and zinc chloride solution was performed on a hotplate stirrer at 300 rpm at 80 °C, completely dried in an oven at 110 °C, and pounded with a mortar. Subsequently, the chemically impregnated powder obtained was converted into solids coin-like by pressing on a hydraulic press with ±8 metric tons. The samples were solid coins with dimensions of 20 mm diameter, 25 mm height, and 70 mg mass. This was followed by the preparation of 20 solid precursors for high-temperature pyrolysis in a furnace tube. The pyrolysis process was performed in two integrated stages, namely carbonization and physical activation at a temperature ranging from 28 °C to 850 °C in a stream of N_2 and CO_2 gases. Heating from 28 °C to 600 °C was also carried out by flowing N_2 gas at a heating rate of 3 °C/min (carbonization). The gas flow was switched with CO_2 to a maximum temperature of 850 °C at a heating rate of 10 °C/min and cooled at a travel time of 12 h. Finally, the solid-activated carbons obtained were washed using distilled water until neutral pH is obtained. The ILAE-based solid porous carbon (SPC) was labeled as x-ILAE-SPC,

where x with values of 0.3, 0.5, and 0.7 represented the mass ratio of precursor powder/$ZnCl_2$.

2.3. Supercapacitor cell preparation

The supercapacitor cell is designed to resemble a solid coin stack consisting of solid carbon electrodes, current collectors, a separator, an electrolyte, and a body cell. The solid activated carbon based on *Laurus nobilis* was prepared in 9 mm diameter, 0.2 mm thick, and 10 mg active mass as the working electrode. The current collector from stainless steel was made to adjust the electrode surface. The separator was selected from an organic material based on a duck eggshell membrane and a 1 M H_2SO_4 solution was determined as the aqueous electrolyte. The cell bodies are designed to be rectangular in dimensions of 2x3cm, which are perforated with a diameter of 9 mm in the middle. These components are arranged to obtain the supercapacitor cell sandwich layer.

2.4. Material characterization

The carbon density was evaluated by shrinking the dimensions of the solid coin during the heating process. The dimensions of diameter, thickness, and mass were calculated before and after pyrolysis to estimate the density changes during the heating process using a formula in line with a standard equation that has been previously reported [43]. X-ray diffraction (XRD) in the XRD XPERT PRO PANalitycal PW3040/60 instruments was used to examine the phase change properties and crystal structure with Cu Kα radiation sources. The 2θ diffraction angle was selected from 10° to 100° at a scan step of 0.002°. The parameters of interlayer spacing and microcrystalline dimensions were calculated using Braggs law and the Debye-Scheerer equation [44,45]. Scanning electron microscopy (SEM) on the JEOL-JSM6510 (LA) instrument was selected as a general method for capturing morphological images of porous carbon surfaces. The constituent elements of *Laurus nobilis* porous carbon were determined using the energy dispersive spectroscopy (EDS) approach in the ZAF Method Standardless Quantitative Analysis with an energy range of 0–20 keV. Porosity properties including specific surface area and pore size distribution were evaluated with the N_2 gas adsorption/desorption isotherms technique in the
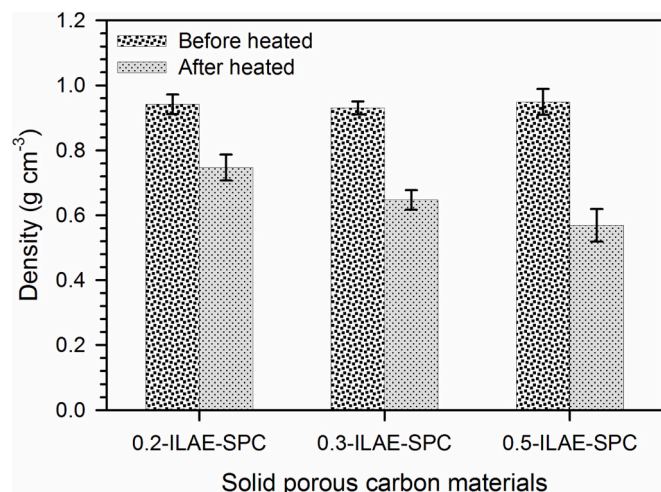
Fig. 1. Reducing density dimension before and after heated treatment.

Quantachrome TouchWin v1.22 instrument at 10.0 °C/min. The specific surface area was evaluated by the BET equation. Meanwhile, the specific micropore surface area was calculated using the T-Plot method, and the pore size distribution was confirmed by the BJH equation.

2.5. Electrochemical measurement

The electrochemical properties of the supercapacitor cells were evaluated in detail through the complete method of cyclic voltammetry (CV), galvanostatic charge-discharge (GCD), and electrochemical impedance spectroscopy (EIS) in a two-electrode system (symmetrical supercapacitor) at room temperature of 30 °C. The aqueous electrolyte was selected as the test electrolyte in 1 M H_2SO_4. The CV test was performed with the CV-RAD-ER 2810 instrument, with error $\pm$ 6.05 at different scan rates from 1 mVs^{-1} to 10 mVs^{-1} in a potential window of 0-1 V. Subsequently, the specific capacitance was calculated based on a standard formula [46,47]:

$$C_{sp} = \frac{2I}{s \times m}$$

where C_{sp} (Fg^{-1}) is the specific capacitance, I (A) is current, s (mV s^{-1}) is the scanning rate, and m (gr) is the working mass. Furthermore, the GCD method was reviewed using the GCD-RAD-ER 2018 instrument (calibrated error $\pm$ 6.05) in a voltage window of 0–1 V at a current density of 1–10 A g^{-1}. Specific capacitance, energy density, and power density are determined by standard equations as expressed below [48,49]:

$$C_{sp} = \frac{I \times \Delta t}{m \times \Delta V}$$

$$E_{sp} = \frac{C_{sp} \times \Delta V^2}{7.2}$$

$$P_{sp} = \frac{3600 \times E_{sp}}{\Delta t}$$

where C_{sp} (F g^{-1}) is the specific capacitance, I (A) is the current, t (s) is the discharge time, m (gr) is the working mass V (V) is a potential
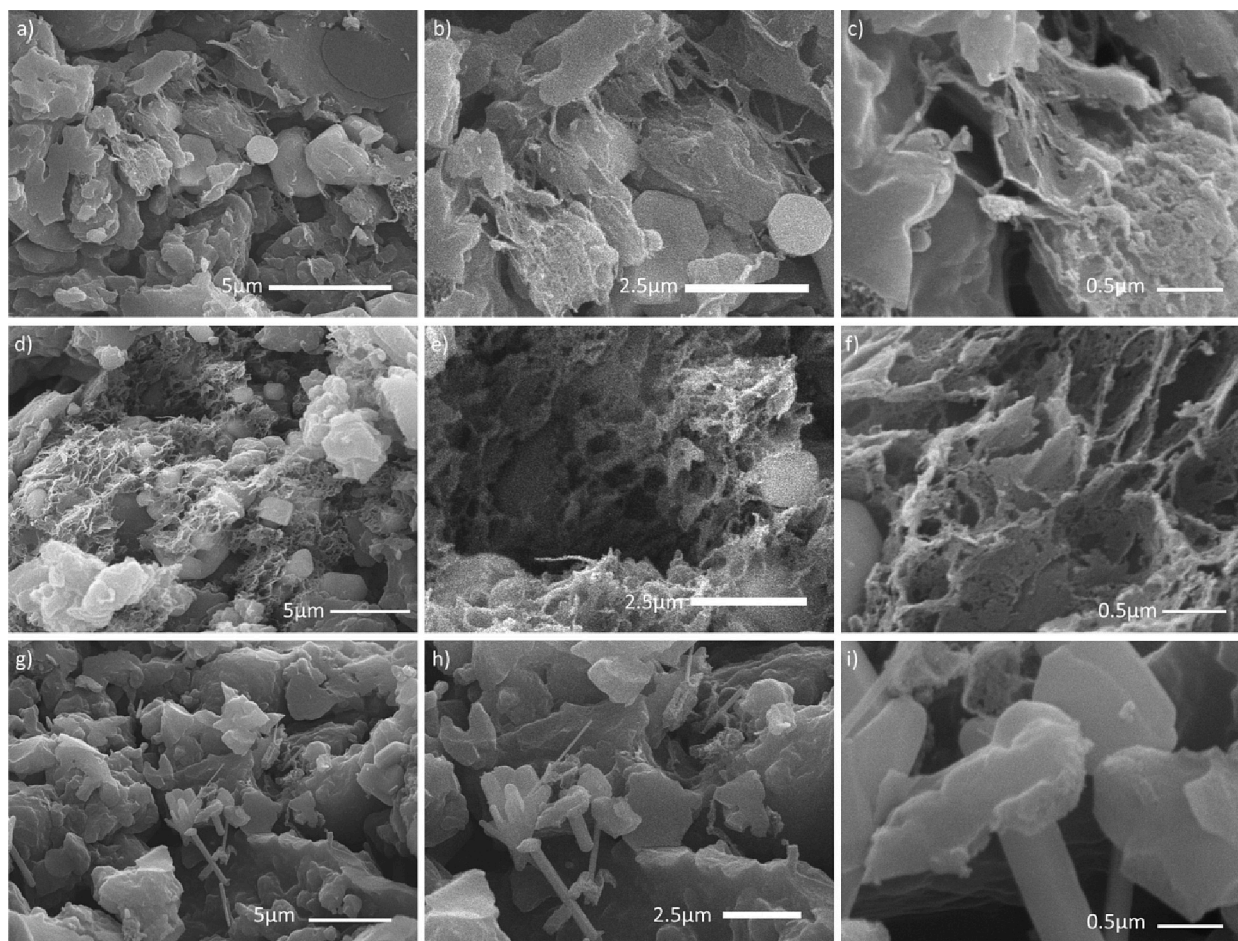

Fig. 2. SEM images of a-c) 0.3-ILAE-SPC, d-f) 0.5-ILAE-SPC, and g-i) 0.7-ILAE-SPC In different zoom.
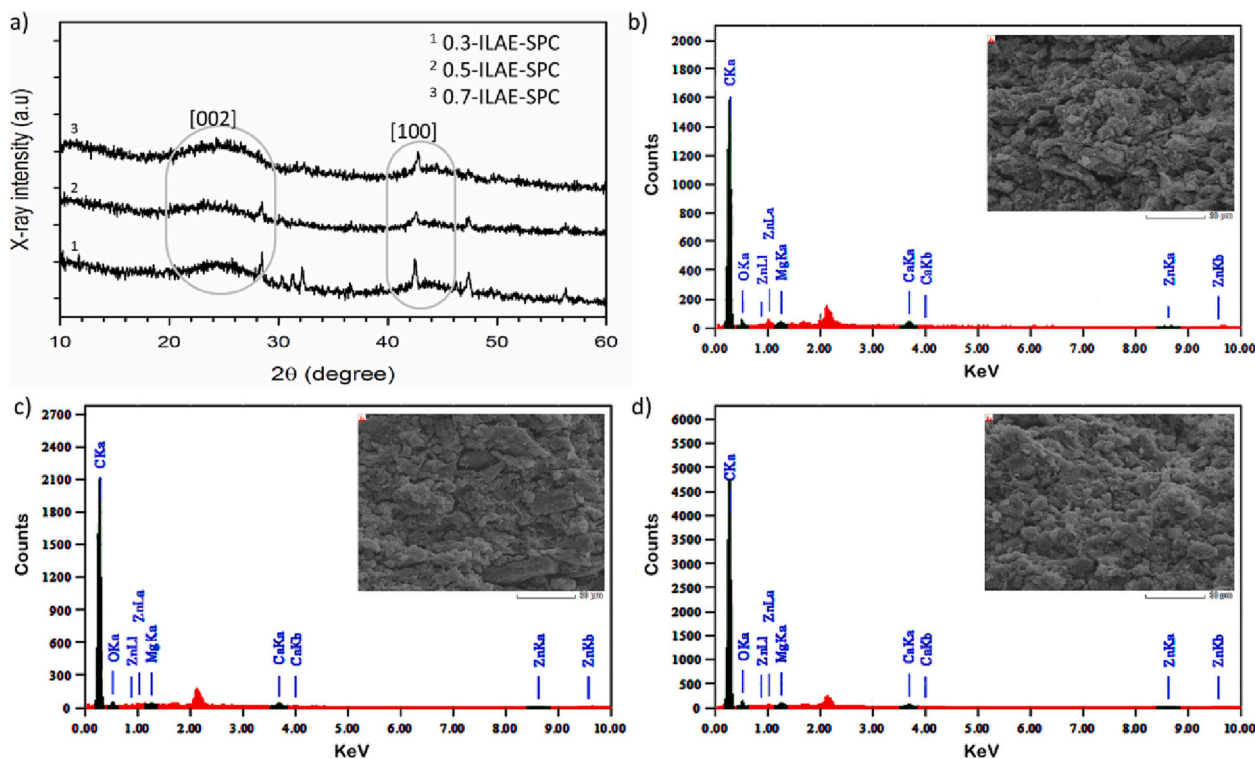
Fig. 3. a) XRD pattern of x-ILAE-SPC, EDS spectra of b) 0.3-ILAE-SPC, c) 0.5-ILAE-SPC, and d) 0.7-ILAE-SPC.

window, E_{sp} (Wh kg^{-1}) is the current density, and P_{sp} (W kg^{-1}) is the power density. The EIS was reviewed using a single-channel electrochemical workstation instrument model CS350 in the frequency range from 100 mHz to 100 kHz. EIS measurement results are processed using CS6 studio software. The preparation of x-ILAE-SPC is shown in Scheme 1.

3. Result and discussions

The multi-activation strategy of carbonization, chemical activation, and physical activation is considered effective, efficient, simple, and free of harmful by-products in obtaining high carbon fixed from biomass which incidentally has complex impurities [50]. Therefore, impurities such as organic compounds, volatiles, water content, and tar must be removed in the synthesis of biomass-based highly pure carbon [51]. These compounds are removed through the selected approach route without corrosive and toxic residue. They can also be assessed early through density changes before and after the treatment in ILAE-based solid carbon precursors as shown in Fig. 1. The x-ILAE-SPC density decreased significantly after the synthesis route was applied. Initially, the precursor densities were about 0.9414, 0.9301, and 0.9489 g cm^{-3} at a standard deviation of 0.02–0.05 for 0.3-ILAE-SPC, 0.5-ILAE-SPC, and 0.7-ILAE-SPC, respectively. The multi-activation strategy begins with the carbonization process from low temperatures which tends to focus on the evaporation of water and volatiles through steam and carbon dioxide [52]. At a temperature range of 250–450 °C, they cleave organic molecules from the hemicellulose and cellulose components [53]. The relatively low lignin component of the ILAE precursor degrades at temperatures higher than 490 °C and the final product possessed a high fixed carbon with relatively low tar and ash [54]. Subsequently, the impregnation of ZnCl$_2$ before the conversion of solid carbon began to react with elemental carbon at a temperature of 500 °C. First, ZnCl$_2$ reacted with oxygen to form zinc oxychloride and etched the carbon chains, enabling the erosion of the skeleton which leaves carbon dioxide evaporated [55]. In general, their chemical reactions can be written as follows:

$$ZnCl_2 + 1/2O_2 \rightarrow ZnOCl + 1/2Cl_2$$

$$2ZnO + C \rightarrow 2Zn + CO_2 \uparrow$$
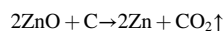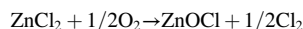
The physical activation involving CO$_2$ at a high temperature of 850 °C significantly removed tar and ash in the precursors initiating the presence of void spaces in the biomass carbon precursors [56]. In simple terms, the interaction between CO$_2$ and C is illustrated as follows:

$$C + CO_2 \rightarrow 2CO$$
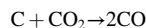
The surface carbon complex can be decomposed and removed in the form of carbon monoxide CO, leaving a free surface carbon that allows the production of pores in the precursor. Finally, the combination of these processes significantly decreased the x-ILAE-SPC, which dropped to 0.7476, 0.6476, and 0.5693 g cm^{-3} at standard deviations of 0.03–0.05 for 0.3-ILAE-SPC, 0.5-ILAE-SPC, and 0.7-ILAE-SPC, respectively. The increase in the ratio of the chemical activating agent ZnCl$_2$ also reduced the density of the precursor from 19.38 % at 0.3-ILAE-SPC to 37.96 % at 0.7-ILAE-SPC. This is due to the relatively high accumulation of carbon chain etching at a higher ZnCl$_2$ ratio, allowing the formation of various pore structures to initiate high void spaces. This analysis serves as an initial guideline for exploring the potential of ILAE as a source of high-porous carbon in sustainable electrode materials.

ILAE is a unique green aromatic biomass precursor as a sustainable carbon source with significant morphological structures as a contribution from their characteristic volatile content. In this study, a chemical impregnation step and a one-stage carbonization-physical activation strategy were proposed to prepare porous carbon nanosheets. The selected synthesis route is considered to maximize the exploitation of their unique morphological structure. A scanning electron microscopy (SEM) technique was prepared to assess a comprehensive understanding of the surface morphology of ILAE-biomass carbon. The SEM micrograph of x-ILAE-SPC is shown in Fig. 2 with various magnifications of the selection area. The precursor with 1:0.3 ratios illustrated a smooth surface structure with block carbon in the range of 0.46 μm to 2.73 μm, as presented in Fig. 2a. This is attributed to the narrow pore growth

Table 1
XRD parameters and element analysis of x-ILAE-SPC.

Carbon porous	Interlayer spacing				Microcrystalline dimensions		Elemental status				
	$2\theta_{002}$ (°)	$2\theta_{100}$ (°)	d_{002} (nm)	d_{100} (nm)	L_c (nm)	L_a (nm)	C (%)	O (%)	K (%)	Mg (%)	Zn (%)
0.3-ILAE-SPC	22.641	44.816	0.3924	0.2020	0.8567	0.8313	93.63	5.23	0.44	0.23	0.48
0.5-ILAE-SPC	24.414	44.078	0.3643	0.2053	0.6726	1.8437	95.07	4.49	0.34	0.10	0.00
0.7-ILAE-SPC	24.701	42.820	0.3601	0.2110	3.7129	1.0329	93.90	5.56	0.19	0.29	0.07

potential and the high conductivity at 0.3-ILAE-SPC, which enables the provision of abundant ion adsorption sites at the supercapacitor electrode/electrolyte interface. When zoomed larger in Fig. 2b, 0.3-ILAE-SPC confirmed the fine/thin sheet morphology adhering to the carbon aggregate. The relatively low ratio of $ZnCl_2$ in its reaction with C only a few macropores in the 200–650 nm range can also be detected at 0.3-ILAE-SPC. This is revealed in Fig. 2c, where the macropores structure is confirmed with thin sheets on their upper surface walls [57]. The macropores texture followed by a thin sheet is beneficial for improving electrochemical performance, because of the increase in massive mass transfer and large surface area for accumulating electrolyte ions [58,59].

By increasing the addition of the $ZnCl_2$ ratio at 1:0.5, the ILAE-derived carbons were converted into 3D porous carbon nanosheets interconnected as local pore walls, as shown in Figs. 2d-2f. Based on combustion and the limited reaction of $ZnCl_2$ and C followed by the decomposition of ZnOCl and further reaction of ZnO with C for activation, the surface morphology of the precursor changed and became rough, which was rich in various pores, as presented in Fig. 2d. Furthermore, 0.5-ILAE-SPC showed a hierarchical pore of abundant macropores and *meso*pores as illustrated in Fig. 2e. From Fig. 2f, 0.5-ILAE-SPC confirmed 2D nanosheet structures with the sheet walls filled with pores forming a gauze-like sheet. The abundance of micro-mesopores on the nanosheet walls formed by $ZnCl_2$ etching and hydrolysis of lignin, cellulose, and volatiles during this combustion process provides abundant transfer routes and interconnected active sites [60]. The detailed micro, meso, and macropores textures of the carbon nanosheets were further investigated through the absorption of N_2 gas as illustrated in Figs. 4–5. The combined morphological structure of hierarchical pores and a gauze-like sheet benefits the electrode material by reducing electron transfer resistance and accelerating the diffusion of the electrolyte to the inner surface of the carbon, potentially leading to improved electrochemical performance [31,61].

Over-etching with increasing $ZnCl_2$ dose at 0.7-ILAE-SPC caused the collapse of the 3D hierarchical pores, followed by erosion of the thin sheets leading to loss of 2D nanotexture. The role of high-temperature pyrolysis processing in excessive ZnCl impregnation allows the

reduction of the unique morphology of the ILAE precursor, as shown in Fig. 2g-i. Based on Fig. 2g, it was discovered that the morphology of 0.7-ILAE-SPC is dominated by large particle aggregates on a macro scale with a relatively flat surface. Moreover, a rod-like structure was displayed at the selected magnification in Fig. 2h. A previous report stated that there is a possibility to erode the walls of lignin and cellulose intensely. The size of this unique morphological structure ranges from 200 nm to 789 nm.

X-ray diffraction (XRD) analysis was adopted to verify the presence of carbons and their structural changes followed by the active phase of ILAE-based solid carbon. As indicated in Fig. 3a, x-ILAE-SPC presents two broad diffraction peaks centered at $2\theta = 22$–$24°$ and 43–$44°$, indexed to the (002) and (100) carbon planes. This characteristic confirms the disturbed semicrystalline structure initiating turbostratic carbon with weak graphitization [62]. The diffraction peak in the carbon 002 plane indicates the presence of low graphitization, while the 100 plane with low intensity indicates abundant amorphism in the solid carbon ILAE precursor. Furthermore, low sharp peaks were also weakly confirmed in the XRD pattern, indicating the relatively low presence of inorganic crystalline compounds such as potassium, magnesium oxide, and zinc oxide compounds. This is in line with the EDS analysis that summarizes the status elements precursor in Table 1. The presence of these impurities is contributed by the basic constituents of ILAE and residues from the $ZnCl_2$ reaction. Previous studies have also confirmed the presence of similar impurities in biomass-based carbon precursors such as porous carbon from banana leaf [63], bamboo [64], and pineapple leaves [65]. Furthermore, the ratio increasing from 0.3-ILEA-SPC to 0.5-ILEA-SPC significantly showed a weak peak area change, which was associated with a carbon layer defect that weakened the crystallinity level and increased abundant pore production. The etching of carbon through $ZnCl_2$ at a ratio of 1:0.5 confirms the irregular structural features with high amorphous. This showed a large specific surface area and abundant pore routes that are important for enhancing the charge storage of the supercapacitor [66]. The presence of the impurity compounds was also significantly reduced, where zinc oxide was completely removed at a ratio of 1:0.5, confirming the effectiveness of the optimal
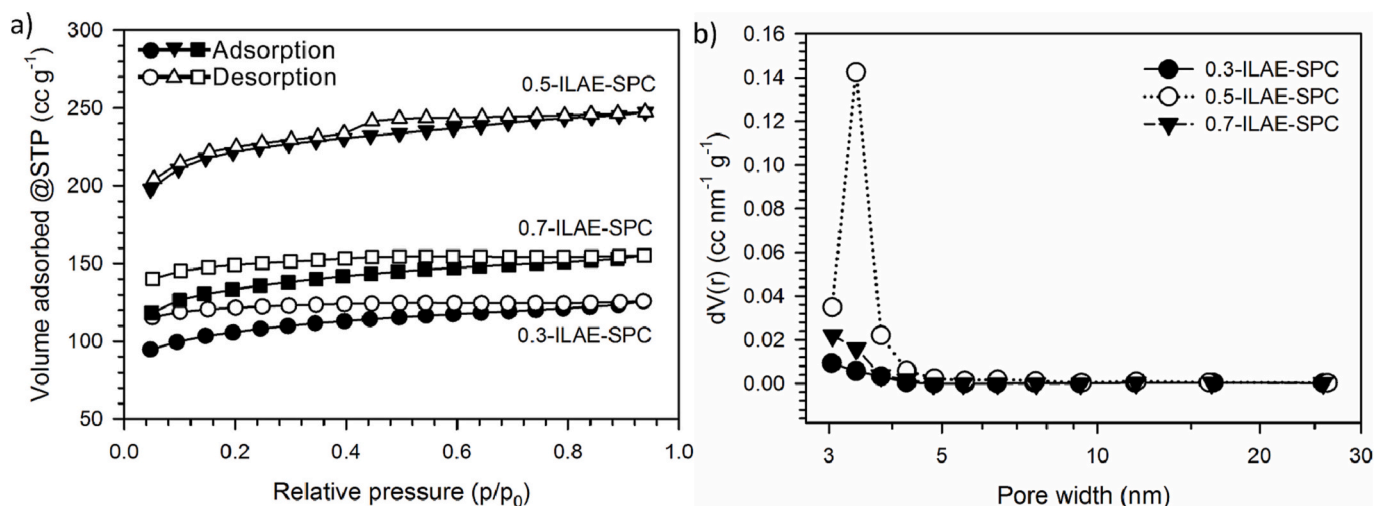

Fig. 4. a) N_2 isotherm adsorption-desorption, and b) mesopores distribution of x-ILAE-SPC.

Table 2

Porosity properties of x-ILAE-SPC.

Samples	S_{BET} (m² g⁻¹)	S_{micro} (m² g⁻¹)	S_{meso} (m² g⁻¹)	V_{tot} (cc g⁻¹)	D_{av} (nm)
0.3-ILAE-SPC	334.697	269.955	64.742	0.194986	1.16515
0.5-ILAE-SPC	689.935	608.195	81.740	0.38371	1.11232
0.7-ILAE-SPC	419.311	339.932	79.378	0.240482	1.14703

chemical reaction to dehydrate organic compounds and their residues. Other impurity compounds also display similar characteristics. The addition of a higher ratio to 0.7-ILAE-SPC illustrates a strong broad peak in the carbon plane (002), associated with semi-crystalline degradation that initiates the presence of a graphite-like carbon structure [67]. This is a strong consideration for the presence of sheet carbon structures in the x-ILAE-SPC precursor.

The interlayer spacing (d_{002} and d_{100}) and microcrystalline dimensions (L_c and L_a) are summarized in Table 1. The d_{002} of x-ILEA-SPC shows values in the range of 0.3601 to 0.3924 nm, which are relatively larger than the d_{002} structure of carbon graphite (0.3354 nm). This revealed that the obtained carbon has an amorphous structure with an abundant presence of pores [45]. Meanwhile, d_{001} ranges from 0.2020

to 0.2110 nm due to the weak crystalline nature of the precursor. The effectiveness of providing suitable active sites accumulated in the surface area can be predicted through the microcrystalline L_c dimension. This is supported by Kumar et al. 1997 and Deraman et al. 2015 [68,69], who stated that the surface area of carbon precursors can be determined through empirical equations. The low L_c allows the provision of a high surface area to the precursor carbon. Therefore, 0.5-ILAE-SPC confirms the precursors' potential in producing high specific surface area, which is very useful in improving the capacitive properties of supercapacitors. An in-depth analysis is reviewed on N_2 gas uptake is in Fig. 4 and Table 2.

The chemical element analysis of the ILAE precursor converted to SPC was reviewed in detail through the energy dispersive spectroscopy (EDS) technique, as illustrated in their spectra (Fig. 3b-d). Table 1 summarizes the x-ILAE-SPC status elements obtained from $ZnCl_2$ impregnation at different ratios in high-temperature heated treatment. The selected porous carbon conversion strategy possessed a very high level of carbon purity of 93.63–95.07 % to improve the performance of electrode materials in electrochemical double-layer capacitor (EDLC) systems. Furthermore, oxygen was the second highest element in the impregnation range of 4.49 % to 5.56 %, which is closely related to their contribution to providing wettability properties of x-ILAE-SPC. The high wettability significantly contributes to the presence of faradaic redox reactions in the electrode material [70]. This confirms the potential of the precursors to exhibit pseudo-capacitive behavior in the
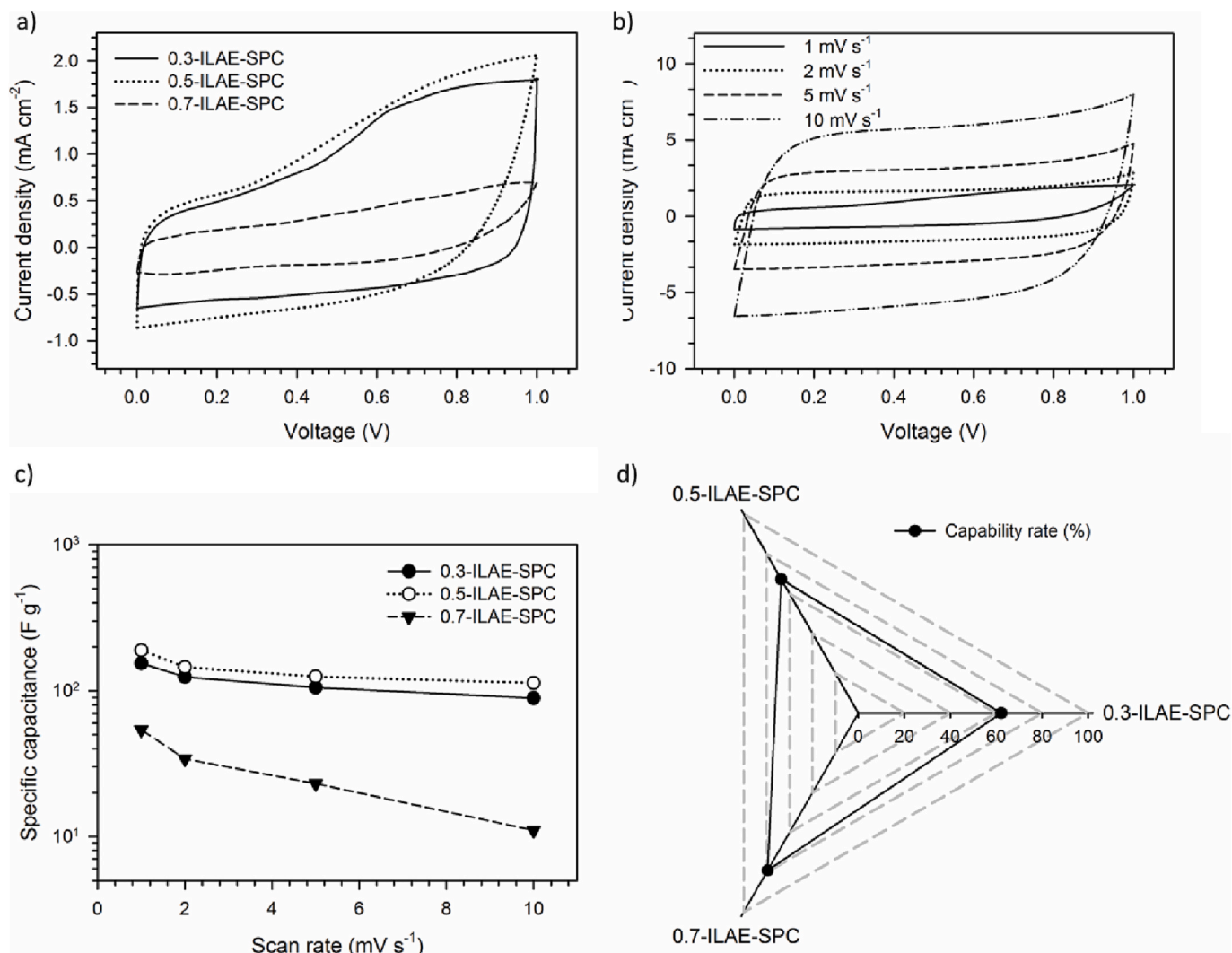
Fig. 5. a) CV profile in 1 mVs⁻¹ of x-ILAE-SPC, b) CV profile in 1–10 mV s⁻¹ of 0.5-ILAE-SPC, c) specific capacitance vs. different scan rate, and d) cyclic pervormance in 1–10 mVs⁻¹ of x-ILAE-SPC.

electrochemical properties [25,71]. $ZnCl_2$ also vaporizes organic compounds, impurities, and ash maximally in precursors to obtain good biochar. The increase in the impregnation ratio also leads to higher carbon purification with optimum reduction of Mg and K impurities in the range of 0.44 % to 0.10 %. The Zn residues were completely removed at 0.5-ILAE-SPC followed by the degradation of their impurities. Meanwhile, an increase in the $ZnCl_2$ ratio at 0.7-ILAE-SPC caused a carbon reduction of 93.90 %, associated with an excessive carbon etching reaction. This is described in Table 1 where the excessive removal of the pore framework reduces purity and increases elemental oxygen in the precursor.

The porosity behavior and pore distribution characteristics of carbon nanosheets based on aromatic evergreen *Laurus nobilis* leaves were evaluated by N_2 isotherm adsorption-desorption at 77 K, as illustrated in Fig. 3a. The N_2 adsorption isotherm profile of the x-ILAE-SPC mainly shows the prominent combination features of the type-I and IV curves. This is characterized by a drastic increase in the adsorbed volume at a relatively low-pressure region (P/P0 < 0.049), proving the presence of abundant micropores (type I). A weak hysteresis loop on the isotherm (P/P0 > 0.31) also indicates the presence of a confirmed rapidly growing mesoporous minority, namely type IV [72]. The nature of the micro-mesoporous combination stems from the release of small molecules of characteristic aromatic volatiles during the decomposition of the lignocellulosic components upon activation of $ZnCl_2$. Recently, many theories have reported that the dominant micropores significantly promote the electrochemical double-layer abnormal capacitance (EDLC) enhancement in carbon materials [66,73]. The larger mesopore size

enables the carbon material to enhance the fast accessibility and high power density of supercapacitor devices [74]. Furthermore, x-ILAE-SPC displays two distinct pore types, namely micropores and mesopores which simultaneously contribute to the enhancement of EDLC by providing suitable active sites for electrolyte ions and reduced ion transfer resistance for fast dynamic charging processes. The 0.3-ILAE-SPC shows a hysteresis loop profile with longer open tails revealing poor mesoporous development with a narrow-bottleneck-like pore structure. This imperfect pore pattern impedes the desorption of N_2 gas to distort the isotherm profile, with a specific surface area ranging from 334.697 $m^2\,g^{-1}$ at a total volume of 0.194 $cm^3\,g^{-1}$. The addition of the $ZnCl_2$ ratio showed a significant specific surface area of 689.935 $m^2\,g^{-1}$ and a total volume increase of 0.38371 at 0.5-ILAE-SPC. The relatively closed hysteresis loop profile characterizes the development of a well-defined mesoporous structure with a unique morphology of nanosheets. The result showed that confirmed mesoporous structure in the nanosheet morphology as an open channel can reduce the ion-electrode resistance and increase fast ion migration ability to reduce the shrinkage effect of capacitive behavior at large current densities. As presented in Table 1, the ratio of $ZnCl_2$ 1:0.5 yielded the highest specific surface area in ILAE-SPC with a predominance of 88 % microporous and 12 % mesoporous, causing a significant increase in electrochemical behavior. Moreover, a greater increase in the ratio at 0.7-ILAE-SPC did not guarantee the formation of high porosity. The carbon surface area was reduced to 419.311 $m^2\,g^{-1}$ with the total volume maintained at 0.24048 $cm^3\,g^{-1}$. Chemical impregnation at higher solution concentrations was found to cause shrinkage of the carbon skeletons and damage nanosheet

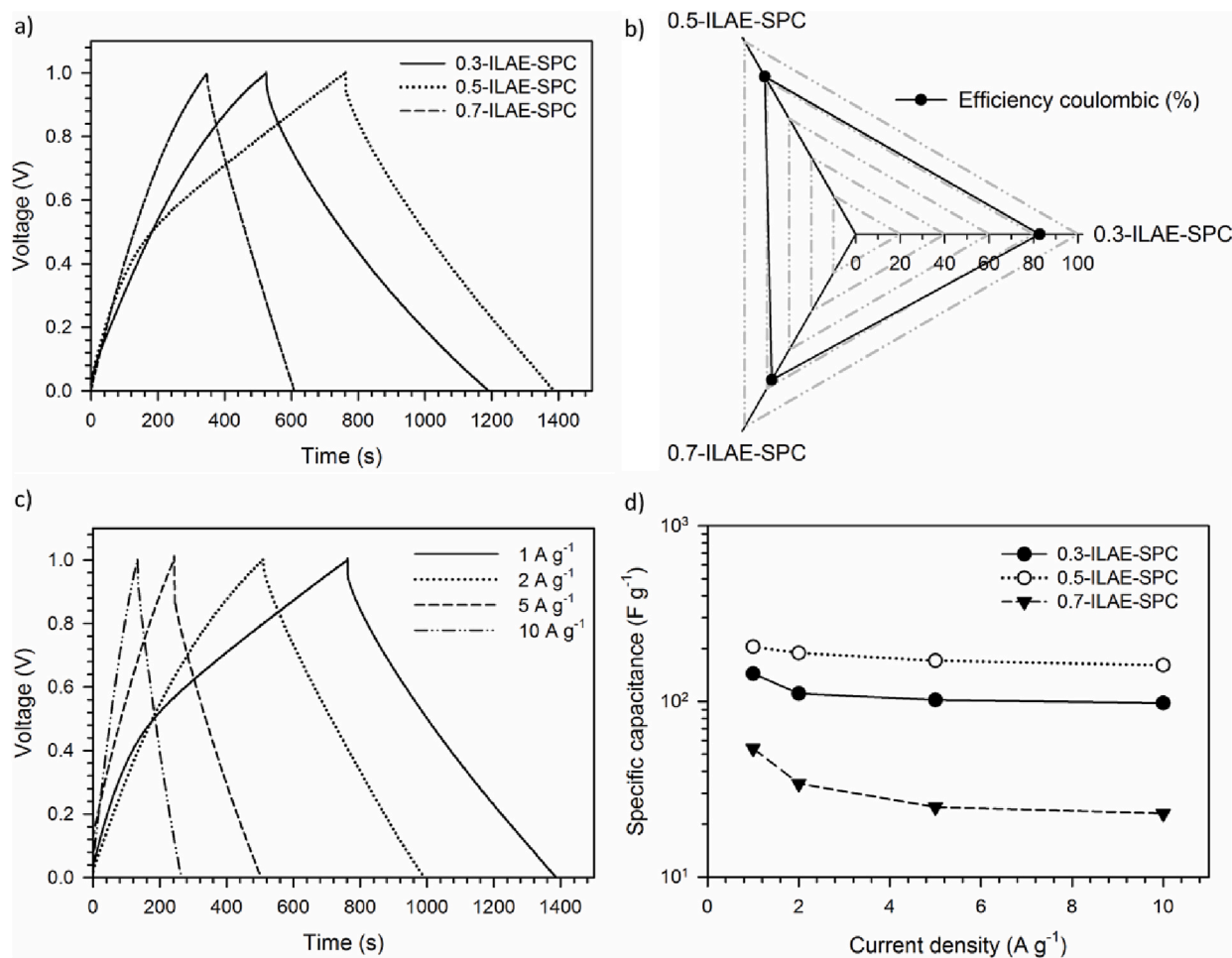**Fig. 6.** a) GCD profile in 1 A g^{-1} of x-ILAE-SPC, b) GCD profile in 1–10 A g^{-1} of 0.5-ILAE-SPC, c) specific capacitance vs. different current density, and d) coulombic effiency in 1–10 A g^{-1} of x-ILAE-SPC.

morphology. This leads to a decrease in surface area and a reduction in the electrochemical performance.

To confirm mesopores in x-ILAE-SPC, their pore size distribution was reviewed in detail by adopting the BJH method, as illustrated in Fig. 3b. It was discovered that all samples show a clear mesoporous presence in the 3.0-28 nm size range. Meanwhile, 0.5-ILAE-SPC gave the highest mesoporous volume confirming the rapid development in carbonaceous materials. This feature is needed to achieve maximum ion accessibility in the electrode material. Further analyzes were confirmed through the CV and GCD approaches.

The electrochemical performance of ILAE-based carbon electrodes was studied comprehensively in a symmetrical supercapacitor system with an aqueous electrolyte of 1 M H_2SO_4. Firstly, the 0.3-ILAE-SPC, 0.5-ILAE-SPC, and 0.7-ILAE-SPC electrodes were evaluated at 1 mV s^{-1} cyclic. As presented in Fig. 5a, the CV profile showed a nearly perfect rectangular shape revealing the purely electrochemical properties of the charge interactions at the electrode/electrolyte interface [75]. More specifically, the x-ILAE-SPC electrode has a significant increase in current density a "camel's hump-like" at a potential window of 0.4–0.8. This is closely related to the faradaic redox reaction characterizing the pseudo-capacitance effect, which is the contribution of self-doping oxygen heteroatoms [76]. Previous investigations have established that oxygen content always accompanies the synthesis of porous carbon because the dangling carbon bonds are known to absorb moisture quickly [77]. This was confirmed in detail on XRD and EDS analyses, as shown in Fig. 2 and Table 1. The oxygen functional group has a significant impact on the charge storage properties of the porous carbon. This makes oxygen functionalization receive much attention to improve the properties of carbon-based energy storage electrodes. Therefore, the camel's hump on the CV profile is confirmed in the 0.4–0.8 V range. According to the electrical double-layer properties and pseudocapacitance effect, the 0.3-ILE-SPC electrode displays a specific capacitance of 144 F g^{-1} in a two-electrode configuration system. The increase in the ratio of the activating agent to 1:0.5 significantly increased its capacitive properties by 189 F g^{-1}. The morphological structure of 2D nanosheets with their sheet walls filled with pores forming a gauze-like sheet at 0.5-ILAE-SPC enables rapid adsorption-desorption of ionic charges, thereby enhancing the super-capacitive properties of the porous carbon [78]. The confirmed self-oxygen doping caused an increase in the performance of the electrode material. However, increasing the ratio higher at 1:0.7 indicates degradation of the carbon electrochemical properties. 0.7-ILAE-SPC illustrates a small CV profile with a distorted shape confirming the weaker electrochemical properties. Although the oxygen functionalization increased to 5.56 %%, the unfavorable pore structure in the SEM image followed by the majority of micropores weakened the accessibility of charged electrolyte ions on the carbon electrode surface, which impacts their electrochemical performance [66]. The capacitive properties obtained are highly reduced with a specific capacitance of 145 F g^{-1}. Moreover, the specific capacitance of x-ILAE-SPC is relatively much higher than porous carbon based on ILAE without activation which only has a specific capacitance of 36 F g^{-1}, as illustrated in Fig. S1a.

The confirmation of the high performance of the 0.5-ILAE-SPC electrode was reviewed by the CV curve in the higher scan rates from 1 mV s^{-1} to 10 mV s^{-1}, as shown in Fig. 5b. It was discovered that the CV profiles retain a rectangular shape, indicating good double-layer capacitive properties. In addition, CV curves of 0.5-ILAE-SPC still maintan rectangular shape in 100 mV s^{-1}, as illustrated in Fig. S2. The effect of pseudo-capacitance was also missing, indicating that the self-doping of the provided heteroatoms was insufficient to sustain the faradaic redox reaction at a high scan rate of 10 mV s^{-1}, as stated in previous literature [76]. Furthermore, an increase in scanning rate caused an evaluation of the specific capacitance of the carbon electrode. Fig. 5c displays the specific capacitances obtained by the x-ILAE-SPC electrodes at different scanning rates. The results showed that increasing the scanning rate from 1 to 10 mV s^{-1} significantly degrades the

capacitive properties of the electrode material. This is due to the pore structure of the electrode material is not completely accessible to electrolyte ions [79]. The conductivity of the electrolytes and resistance are also considered. However, the three electrodes showed high cyclic performance of 82.45 %, 81.16 %, and 75.45 % for 0.3-ILAE-SPC, 0.5-ILAE-SPC, and 0.70-ILAE-SPC, respectively, as presented in Fig. 5d. Furthermore, the 2D nanosheets followed by a hierarchical pore structure significantly improve the electrode material's performance for supercapacitor applications.

The electrochemical properties of the x-ILAE-SPC electrode were further measured using a galvanostatic charge-discharge technique at a current density of 1 A g^{-1} in a 2-electrode configuration, as presented in Fig. 6a. The GCD profiles of the 0.3-ILAE-SPC, 0.5-ILAE-SPC, and 0.7-ILAE-SPC electrodes confirmed the nearly isosceles triangular shape revealing the electrochemical properties of normal double-layer capacitors. The iR drop was observed to be very weak, indicating the equivalent series resistance of the electrodes obtained by a small delay of approximately 28, 21, and 9 mΩ for the 0.3-ILAE-SPC, 0.5-ILAE-SPC, and 0.7-ILAE-SPC electrodes, respectively. This shows that the addition of an activating agent ratio from 1:0.3 to 1:0.7 significantly increases the accessibility of charged ions through the nano-sheets filled with mesh pores, leading to low resistance and high conductivity [80]. Furthermore, the rapidly expanding pore structure allows the provision of a smooth charge transfer pathway in the supercapacitor cell system, as confirmed in the N_2 gas sorption analysis. The introduction of heteroatomic oxygen dopants onto the carbon surface was significant in the GCD profile, which displays convex and concave curvature in the charging and discharge areas, respectively. Ionic degradation and faradaic reactions of oxygen functional groups significantly affect the ideal GCD profile. The length of time (s) in the charging and discharging process represents the high capacitive nature of the electrode. Based on the standard equation, the specific capacitance obtained was 154, 205, and 144 F g^{-1} with coulombic efficiency of 82.67 %, 81.66 %, and 75.11 % for 0.3-ILAE-SPC, 0.5-ILAE-SPC, and 0.7-ILAE-SPC, respectively, as shown in Fig. 6b. All these capacitive performances were relatively much higher than that of ILAE-based carbon without activation treatment of 43 F g^{-1}, as shown in Fig. S1b.Increasing the impregnation ratio of the $ZnCl_2$ activating agent from 1:0.3 to 1:0.5 also boosted the electrocapacitive 0.5-ILAE-SPC electrode. This is due to a very drastic change in their morphological structure, causing a thin nanosheet structure with sheet walls to overgrow with various pores [57]. This is followed by an increase in the purity of the carbon obtained which initiates high ion accessibility, provision of suitable surfaces, and charge-discharge space [81]. The heteroatom dopant on the carbon surface also serves as an effective linking element for the growth of the hetero-nano structure and helps to achieve higher electrolytic ion adsorption than in pure carbon, chemically active site, wettability, porosity, charge distribution, charge density, conductivity, and electricity [25]. The result also reveals that the contribution of quantum, space charge, and pseudocapacitance leads to a significant improvement of the supercapacitive properties of the carbon structure to improve the supercapacitor performance of the active electrode. However, increasing the ratio of $ZnCl_2$ to 1:0.7 exhibited poor capacitive properties due to significant degradation of porosity and surface morphology followed by a decrease in their carbon content, as confirmed in SEM and EDS images. The over-etching of the carbon chains by the activating agent significantly reduces the hetero-nano structure of the carbon skeleton. This makes the pore structure disintegrate, thereby eliminating the accessibility of ionic charges on the electrode surface. Interestingly, although 0.7-ILAE-SPC has a greater specific surface area than 0.3-ILAE-SPC, 0.3-ILAE-SPC possesses a higher specific capacitance of 154 F g^{-1}. This is due to the mesoporous growth of 0.3-ILAE-SPC which increased by 24.6 % followed by the confirmed hierarchical nanosheet structure that allows for excellent ion transfer at the electrolyte/electrode interface. The GCD curve shape of the 0.5-ILAE-SPC electrode maintains an isosceles triangle shape with high coulomb efficiency at different current
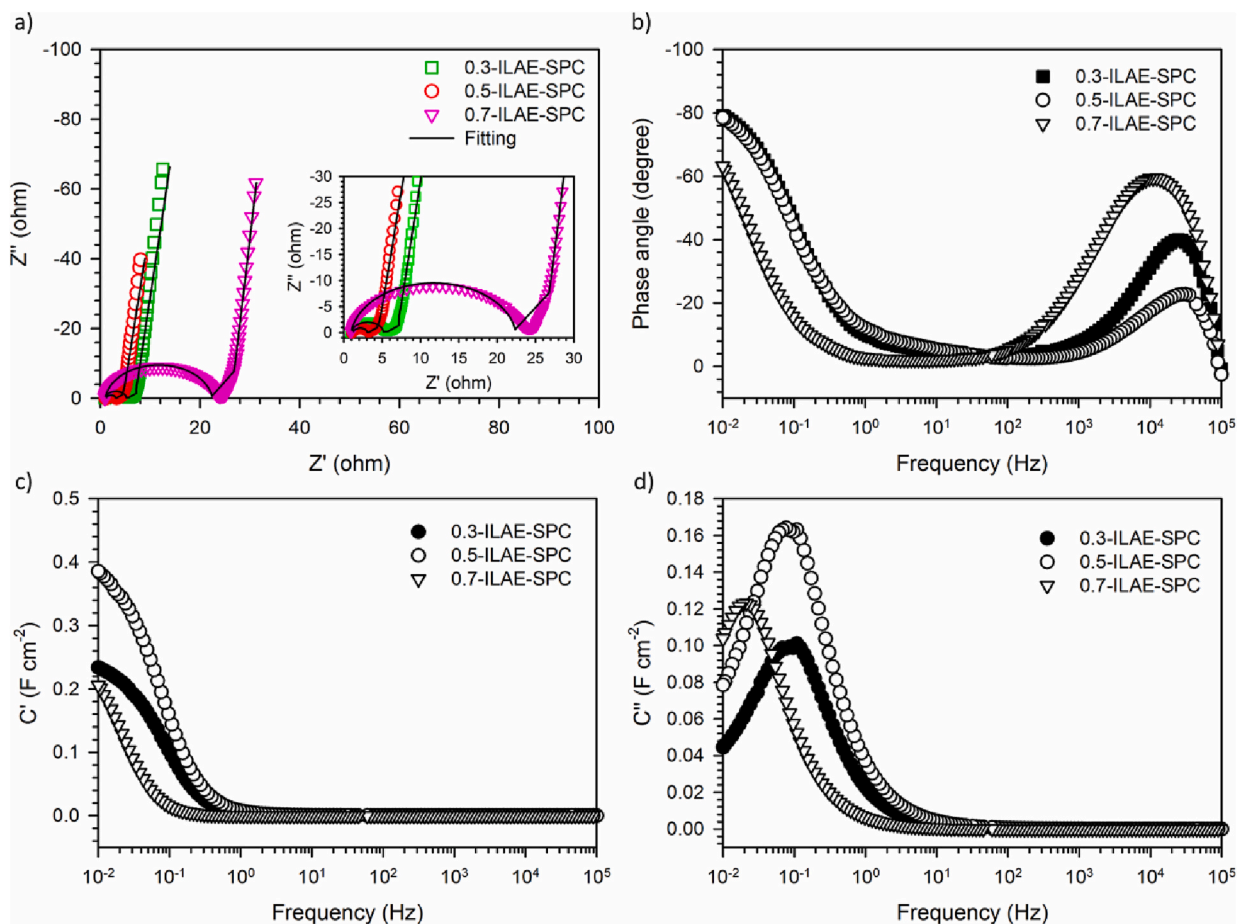
Fig. 7. a) Nyquist plot, b) Bode phase plot, c) Bode plot of real capacitance vs. frequency, and d) Bode plot of imaginer capacitance vs. frequency of x-ILAE-SPC.

densities from 1 to 10 A g^{-1}, indicating the best electrode quality, as illustrated in Fig. 6c. Furthermore, Fig. 6d reveals the specific capacitance of the x-ILAE-SPC electrodes at different current densities. It was discovered that the specific capacitance significantly decreased as the current density increased from 1 to 10 A g^{-1}, due to the non-optimal combination of pore structures reducing the absorption of ionic charge. The carbon electrodes obtained maintained their high capacitive of 98, 161, and 23 F g^{-1} at 10 A g^{-1} for 0.3-ILAE-SPC, 0.5-ILAE-SPC, and 0.7-ILAE-SPC, respectively.

The intrinsic electrochemical behavior of the x-ILAE-SPC electrode was further investigated using electrochemical impedance (EIS) in 1 M H$_2$SO$_4$ electrolyte. The Nyquist plot of the ILAE-based carbon electrode as shown in Fig. 7a confirms the characteristic features of EDLC-type supercapacitors. In addition, the Nyquist plot is fitted using the Randles equivalent circuit. Specifically, the near-perfect vertical line in the low-frequency region illustrates the electrical double-layer response dominance. The striking Warburg curve observable in the insert of Fig. 7a over the intermediate frequency range characterizes the fluctuating diffusion of electrolyte ions into the internal pore channels of the electrode material. Small semicircles in the high-frequency region Nyquist plot reveal a fast charge transfer process, with a significant effect on the relatively fast charge/discharge. The electrolyte resistance of the Nyquist curve is relatively low 0.09, 0.14, and 0.23 Ω for the 0.3-ILAE-SPC, 0.5-ILAE-SPC, and 0.7-ILAE-SPC electrodes, respectively. This is closely related to the porosity and oxygen functional groups at the optimized carbon surface [82]. The real axis intercept is also the equivalent series resistance (ESR), which reflects the electronic resistance of the active material, the contact resistance at the electrode/electrolyte interface, and the electrolyte ion resistance [83]. The increase in the carbon:ZnCl$_2$ ratio from 1:0.3 to 1:0.5 indicates a lower

equivalent series resistance from 0.79 Ω to 0.31 Ω due to significant changes in the morphological structure of rich nanosheet and an improvement in the combination of hierarchically connected micromesopores. The pores on the nanosheets allow fast ion transfer between the sheets to reduce the resistance of the electrode material. The result also showed that the self-oxygen doped allows for an increase in the wettability of the electrode material needed to attract the electrolyte charges at their interface. However, the increase in the ratio of activating agents at 0.7-ILAE-SPC showed a significant increase in the equivalent series resistance of 3.49 Ω. This is due to the reduction of their 2D nanosheet morphological structure, as confirmed via SEM images. The porosity of the activating agents is also graded, thereby allowing closed ionic charge transfer pathways and inhibiting the electrochemical performance of the electrode material. Bode plots have also been studied to evaluate the phase angle-frequency relationship of the proposed ILAE-based carbon electrode. Fig. 7b presents the phase angle of each electrode concerning frequency, where 0.5-ILAE-SPC shows a value of approximately $-80°$ which confirms the ideal capacitive behavior of EDLC with minimum resistance to charge transfer and high capacitive properties [24,84]. Similarly, Bode plots of real capacitance (C') and imaginary capacitance (C'') as a function of frequency were also reviewed on the x-ILAE-SPC electrodes as presented in Fig. 7c and d. Every electrode illustrated a different real capacitance response. The 0.5-ILAE-SPC electrodes display a high C' at low frequencies revealing that their entire surface is accessible to electrolyte ions. The gradual decrease in C' at high frequencies confirms the effective ion adsorption/desorption phenomenon. This proves that spilled microporosity is very necessary to achieve higher performance. Fig. 3d presents C'' as a frequency function that represents the relaxation time constant. Meanwhile, the peak frequency (f$_p$) observed in plot C'' reveals the efficiency
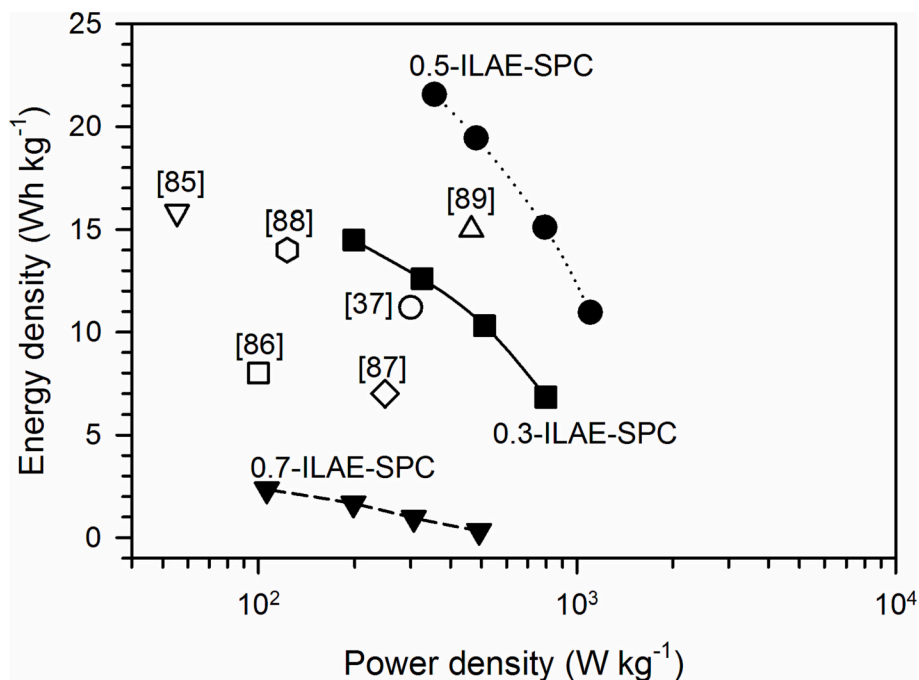
Fig. 8. Ragone plot of x-ILAE-SPC compared with other carbon sources such as pecan shell [37], eggplant [85], quinone amine [86], chitosan [87], corn stalk [88], and Medula tetrapanacis [89].

Table 3
Comparison of the electrochemical behaviors of carbon-based supercapacitors in aqueous electrolytes.

Carbon sources	Structures	Heteroatom	Current density (A g^{-1})/ Electrode system (2-E/3-E)	C_{sp} (F g^{-1})	E_{sp} (Wh kg^{-1})	P_{sp} (W kg^{-1})	Ref
Oak nutshell	Nanosheet	S	0.4/3-E	398	17	200	[23]
Oak nutshell	Nanosheet	S	0.1/2-E	124	–	–	[23]
Eucalyptus-bark	Hierarchical	–	1.4/2-E	155	32.8	57 k	[24]
Alfalfa flowers	hollow structure	O	1.0/2-E	201.4	28	100	[25]
cornstalk pith	Hierarchical	N	0.2/2-E	377	13.2	99.3	[26]
Watermelon peel	Hierarchical	O	1.0/2-E	226	25.4	180	[28]
native European deciduous trees	Hierarchical	–	0.25/3-E	24	0.53	51	[29]
Raw cork	Honeycomb	N	1.0/3-E	180	6.25	259	[90]
Borassus flabellifer fruit Flesh	Hierarchical	–	1.0/3-E	159	8	–	[91]
Borassus flabellifer fruit skin	Hierarchical	–	1.0/3-E	208	–	–	[92]
0.5-ILAE-SPC	Hierarchical-Nanosheet	O	1.0/2-E	205	21.56	1.101 k	Current study

of discharge and charge times at the electrode/electrolyte interface. Based on Fig. 7d, the 0.5-ILAE-SPC electrode showed the shortest relaxation time followed by 0.3-ILAE-SPC, and 0.7-ILAE-SPC 11.91, 24.63, and 62.50 ms, respectively. These results indicate that the 2D nanosheet structure associated with rich micropores and hierarchically linked 3D mesopores significantly contributes to increasing ultra-fast and excellent ion adsorption/desorption capability at the 0.5-ILAE-SPC symmetrical electrode.

An in-depth analysis of the potential application of energy storage devices from a 2D nanosheet-3D hierarchical porous carbon source based on ILAE was also reviewed through a Ragone plot as shown in Fig. 8. It was generally discovered that the energy densities have an ideal range of values for supercapacitor applications and 0.5-ILAE-PC was found to have the most outstanding performance with the highest increased energy density of 21.56 Wh kg^{-1} at a power density of 1.101 KW kg^{-1}. Moreover, the energy density obtained in the two-electrode configuration system was relatively high compared to those reported in previous studies as summarized in Table 3.

4. Conclusion

Novel ILAE biomass was successfully converted into a highly activated carbon 2D nanosheet structure, which is connected hierarchically in 3D and doped with oxygen heteroatoms to optimize the performance of symmetric supercapacitors. Morphological control focused on the ratio of ZnCl$_2$ activating agent at 1:0.3, 1:0.5, and 1:0.7 in high-temperature pyrolysis. The wettability of the carbon obtained was confirmed in the maximum oxygen functional group of 5.56 % which is closely related to self-doping in the pseudo-capacitance effect. Furthermore, 0.5-ILAE-SPC showed optimal porous carbon production with abundant 2D nanosheet structure connecting 3D hierarchical gauze-like sheets. The porosity properties were improved optimally with the highest specific surface area of 689.935 m^2 g^{-1} dominated by micropores of 608.195 m^2 g^{-1} and mesopores of 81.740 m^2 g^{-1} with a total volume of 0.383 cm^3 g^{-1}. The electrochemical properties of the prepared porous carbon were examined in an aqueous electrolyte of 1 M H$_2$SO$_4$ at a potential of 0 V to 1.0 V. Activated carbon nanosheet obtained from the ratio 1:0.3, 1:0.5, and 1:0.7 performed high specific

capacitances of 154, 205, and 44 F g^{-1} with coulombic efficiency of 82.67 %, 81.66 %, and 75.11 % at 1 A g^{-1}, respectively. The 0.5-ILAE-SPC also has the lowest equivalent series resistance of 0.31 Ω proving a very fast ion charge-discharge transfer at the electrolyte/electrode interface. Moreover, the high energy density of 26.30 Wh kg^{-1} at a maximum power density of 1.09 kW kg^{-1} proves that activated carbon nanosheets from Novel ILAE biomass have great potential as sustainable electrodes for clean energy storage devices, especially symmetric supercapacitors.

CRediT authorship contribution statement

Erman Taer: Conceptualization, Methodology, Data curation, **Apriwandi:** Formal analysis, Data curation, Writing- Original draft preparation, Writing- Reviewing & Editing, **Windasari:** Resources, Formal analysis, **Rika Taslim:** Visualization, Validation, Data curation, Mohamad Deraman: Conceptualization, Validation, Data curation.

Declaration of competing interest

The authors declare the following financial interests/personal relationships which may be considered as potential competing interests: Rika Taslim reports was provided by State Islamic University Sultan Syarif Kasim Faculty of Science and Technology. Rika Taslim reports a relationship with State Islamic University Sultan Syarif Kasim Faculty of Science and Technology that includes: employment. Rika Taslim has patent pending to.

Data availability

Data will be made available on request.

Acknowledgements

Appendix A. Supplementary data

Supplementary data to this article can be found online at https://doi.org/10.1016/j.est.2023.107567.

References

[1] F. Perera, Pollution from fossil-fuel combustion is the leading environmental threat to global pediatric health and equity: solutions exist, Int. J. Environ. Res. Public Health 15 (2018) 16, https://doi.org/10.3390/ijerph15010016. Comment.

[2] M. McLennan, S. Group, Zurich Insurane Group, The Global Risks Report 2022 17th Edition, World Economic Forum, 2022.

[3] H. Deng, Y. Tu, H. Wang, Z. Wang, Y. Li, L. Chai, W. Zhang, Z. Lin, Environmental behavior, human health effect, and pollution control of heavy metal (loid)s toward full life cycle processes, Eco-Environ.Health 1 (2022) 229–243, https://doi.org/10.1016/j.eehl.2022.11.003.

[4] R.E.A. Almond, M. Grooten, D.Juffe Bignoli, T. Petersen, Living Planet Report 2022– Building a Nature-positive Society, WWF, Gland, Switzerland, 2022.

[5] U.N.E.P. (UNEP), 21 Issues for the 21 Century Results of the UNEP Foresight Process on Emerging Environmental Issues, United Nations Environment Programme (UNEP), Nairobi, Kenya, 2012.

[6] K. Szocik, M. Braddock, Bioethical issues in human modification for protection against the effects of space radiation, Space Policy 62 (2022), 101505, https://doi.org/10.1016/j.spacepol.2022.101505.

[7] A.D. Sakti, P. Rohayani, N.A. Izzah, N.A. Toya, P.O. Hadi, T. Octavianti, W. Harjupa, R.E. Caraka, Y. Kim, R. Avtar, N. Puttanapong, C.H. Lin, K. Wikantika, Spatial integration framework of solar, wind, and hydropower energy potential in Southeast Asia, Sci. Rep. 13 (2023) 1–18, https://doi.org/10.1038/s41598-022-25570-y.

[8] L. De Souza, N. Simas, D. Bogdanov, P. Vainikka, C. Breyer, Hydro, wind and solar power as a base for a 100% renewable energy supply for South and Central America, PLoS ONE 12 (2017) 1–28, https://doi.org/10.1371/journal.pone.0173820.

[9] T.A. Hamed, A. Alshare, Environmental impact of solar and wind energy - a review, J. Sustain. Dev. Energy Water Environ. Syst. 10 (2022) 1–23.

[10] M.Y. Worku, Recent advances in energy storage systems for renewable source grid integration: a comprehensive review, Sustainability 14 (2022) 5985.

[11] A. Alem, T. Kalogiannis, J. Van Mierlo, M. Berecibar, A comprehensive review of stationary energy storage devices for large scale renewable energy sources grid integration, Renew. Sust. Energ. Rev. 159 (2022), 112213, https://doi.org/10.1016/j.rser.2022.112213.

[12] M.R. Chakraborty, S. Dawn, P.K. Saha, J.B. Basu, T.S. Ustun, A comparative review on energy storage systems and their application in deregulated systems, Batteries 8 (2022) 124.

[13] J. Castro-gutiérrez, A. Celzard, V. Fierro, Energy storage in supercapacitors: focus on tannin-derived carbon electrodes, Front. Mater. 7 (2020) 1–25, https://doi.org/10.3389/fmats.2020.00217.

[14] S. Saini, P. Chand, A. Joshi, Biomass derived carbon for supercapacitor applications: review, J. Energy Storage 39 (2021), 102646, https://doi.org/10.1016/j.est.2021.102646.

[15] X. Li, J. Zhang, B. Liu, Z. Su, A critical review on the application and recent developments of post-modified biochar in supercapacitors, J. Clean. Prod. 310 (2021), 127428, https://doi.org/10.1016/j.jclepro.2021.127428.

[16] Poonam, K. Sharma, A. Arora, S.K. Tripathi, Review of supercapacitors: materials and devices, J. Energy Storage 21 (2019) 801–825, https://doi.org/10.1016/j.est.2019.01.010.

[17] E. Taer, A. Apriwandi, N. Nursyafni, R. Taslim, Averrhoa bilimbi leaves-derived oxygen doped 3D-linked hierarchical porous carbon as high-quality electrode material for symmetric supercapacitor, J. Energy Storage 52 (2022), 104911, https://doi.org/10.1016/j.est.2022.104911.

[18] Z.S. Iro, C. Subramani, S.S. Dash, A brief review on electrode materials for supercapacitor, Int. J. Electrochem. Sci. 11 (2016) 10628–10643, https://doi.org/10.20964/2016.12.50.

[19] H. Yang, S. Ye, J. Zhou, T. Liang, Biomass-derived porous carbon materials for supercapacitor, Front. Chem. 7 (2019) 1–17, https://doi.org/10.3389/fchem.2019.00274.

[20] S. Zang, J. Jiang, Y. An, Z. Li, H. Guo, Y. Sun, H. Dou, X. Zhang, A novel porous organic polymer-derived hierarchical carbon for supercapacitors with ultrahigh energy density and durability, J. Electroanal. Chem. 876 (2020), 114723, https://doi.org/10.1016/j.jelechem.2020.114723.

[21] J. Wang, F. Zheng, Y. Yu, P. Hu, M. Li, J. Wang, J. Fu, Q. Zhen, S. Bashir, J.L. Liu, Symmetric supercapacitors composed of ternary metal oxides (NiO/V2O5/MnO2) nanoribbon electrodes with high energy storage performance, Chem. Eng. J. 426 (2021), https://doi.org/10.1016/j.cej.2021.131804.

[22] A.A. Hor, S.A. Hashmi, Optimization of hierarchical porous carbon derived from a biomass pollen-cone as high-performance electrodes for supercapacitors, Electrochim. Acta 356 (2020), 136826, https://doi.org/10.1016/j.electacta.2020.136826.

[23] A. Gopalakrishnan, S. Badhulika, Sulfonated porous carbon nanosheets derived from oak nutshell based high-performance supercapacitor for powering electronic devices, Renew. Energy 161 (2020) 173–183, https://doi.org/10.1016/j.renene.2020.06.004.

[24] N. Yadav, Promila Ritu, S.A. Hashmi, Hierarchical porous carbon derived from eucalyptus-bark as a sustainable electrode for high-performance solid-state supercapacitors, Sustain. Energy Fuels 4 (2020) 1730–1746, https://doi.org/10.1039/c9se00812h.

[25] S. Meng, Z. Mo, Z. Li, R. Guo, N. Liu, Oxygen-rich porous carbons derived from alfalfa flowers for high performance supercapacitors, Mater. Chem. Phys. 246 (2020), 122830, https://doi.org/10.1016/j.matchemphys.2020.122830.

[26] Y. Xi, J. Cao, J. Li, P. Zhang, Y. Zhu, W. Han, High-rate supercapacitor based on 3D hierarchical N-doped porous carbon derived from sustainable spongy cornstalk pith, J. Energy Storage 37 (2021), 102470, https://doi.org/10.1016/j.est.2021.102470.

[27] T. Yu, F. Wang, X. Zhang, G. Lv, H. Lv, J. Wang, Y. Zhai, Typha orientalis leaves derived P-doped hierarchical porous carbon electrode and carbon/MnO2 composite electrode for high-performance asymmetric supercapacitor, Diam. Relat. Mater. 116 (2021), 108450, https://doi.org/10.1016/j.diamond.2021.108450.

[28] P. Zhang, J. Mu, Z. Guo, S.I. Wong, J. Sunarso, Y. Zhao, W. Xing, J. Zhou, S. Zhuo, Watermelon peel-derived heteroatom-doped hierarchical porous carbon as a high-performance electrode material for supercapacitors, ChemElectroChem 8 (2021) 1196–1203, https://doi.org/10.1002/celc.202100267.

[29] A. Jain, M. Ghosh, M. Krajewski, S. Kurungot, M. Michalska, Biomass-derived activated carbon material from native european deciduous trees as an inexpensive and sustainable energy material for supercapacitor application, J. Energy Storage 34 (2021), 102178, https://doi.org/10.1016/j.est.2020.102178.

[30] E. Taer, A. Apriwandi, A. Agustino, M.R. Dewi, R. Taslim, Porous hollow biomass-based carbon nanofiber/nanosheet for high-performance supercapacitor, Int. J. Energy Res. 46 (2022) 1467–1480, https://doi.org/10.1002/er.7262.

[31] A.R. Selvaraj, A. Muthusamy, In-ho-Cho, H.J. Kim, K. Senthil, K. Prabakar, Ultrahigh surface area biomass derived 3D hierarchical porous carbon nanosheet electrodes for high energy density supercapacitors, Carbon 174 (2021) 463–474, https://doi.org/10.1016/j.carbon.2020.12.052. N. Y.

[32] X. Liang, R. Liu, X. Wu, Biomass waste derived functionalized hierarchical porous carbon with high gravimetric and volumetric capacitances for supercapacitors, Microporous Mesoporous Mater. 310 (2021), 110659, https://doi.org/10.1016/j.micromeso.2020.110659.

[33] E. Taer, N. Yanti, W.S. Mustika, A. Apriwandi, R. Taslim, A. Agustino, Porous activated carbon monolith with nanosheet/nanofiber structure derived from the

green stem of cassava for supercapacitor application, Int. J. Energy Res. 44 (2020) 1–14, https://doi.org/10.1002/er.5639.

[34] M. Wu, S. Xu, X. Li, T. Zhang, Z. Lv, Z. Li, X. Li, Pore regulation of wood-derived hierarchical porous carbon for improving electrochemical performance, J. Energy Storage 40 (2021), 102663, https://doi.org/10.1016/j.est.2021.102663.

[35] S. Ghosh, S. Barg, S.M. Jeong, K. Ostrikov, Heteroatom-doped and oxygen-functionalized nanocarbons for high-performance supercapacitors, Adv. Energy Mater. 10 (2020) 1–44, https://doi.org/10.1002/aenm.202001239.

[36] X. Yang, L. Kong, M. Cao, X. Liu, X. Li, Porous nanosheets-based carbon aerogel derived from sustainable rattan for supercapacitors application, Ind. Crop. Prod. 145 (2020), 112100, https://doi.org/10.1016/j.indcrop.2020.112100.

[37] Y. Zhang, C. Wu, S. Dai, L. Liu, H. Zhang, W. Shen, W. Sun, C. Ming Li, Rationally tuning ratio of micro- to meso-pores of biomass-derived ultrathin carbon sheets toward supercapacitors with high energy and high power density, J. Colloid Interface Sci. 606 (2022) 817–825, https://doi.org/10.1016/j.jcis.2021.08.042.

[38] E. Taer, N. Yanti, R. Taslim, A. Apriwandi, Interconnected micro-mesoporous carbon nanofiber derived from lemongrass for high symmetric supercapacitor performance, J. Mater. Res. Technol. 19 (2022) 4721–4732, https://doi.org/10.1016/j.jmrt.2022.06.167.

[39] L. Wang, X. Li, X. Huang, S. Han, J. Jiang, Activated green resources to synthesize N, P co-doped O-rich hierarchical interconnected porous carbon for high-performance supercapacitors, J. Alloys Compd. 891 (2021) 161908, https://doi.org/10.1016/j.jallcom.2021.161908.

[40] A. Alejo-Armijo, J. Altarejos, S. Salido, Phytochemicals and biological activities of laurel tree (Laurus nobilis), Nat. Prod. Commun. 12 (2017) 743–757, https://doi.org/10.1177/1934578x1701200519.

[41] A. Paparella, B. Nawade, L. Shaltiel-Harpaz, M. Ibdah, A review of the botany, volatile composition, biochemical and molecular aspects, and traditional uses of Laurus nobilis, Plants 11 (2022) 1–24, https://doi.org/10.3390/plants11091209.

[42] A.M. Abioye, F.N. Ani, Recent development in the production of activated carbon electrodes from agricultural waste biomass for supercapacitors: a review, Renew. Sust. Energ. Rev. 52 (2015) 1282–1293, https://doi.org/10.1016/j.rser.2015.07.129.

[43] E. Taer, K. Natalia, A. Apriwandi, R. Taslim, A. Agustino, R. Farma, The synthesis of activated carbon nano fiber electrode made from acacia leaves (Acacia mangium wild) as supercapacitors, Adv. Nat. Sci. Nanosci. Nanotechnol. 11 (2020) 25007, https://doi.org/10.1088/2043-6254/ab8b60.

[44] A. Yaya, B. Agyei-Tuffour, D. Dodoo-Arhin, E. Nyankson, E. Annan, D.S. Konadu, E. Sinayobye, E.a. Bayeh, C.P. Ewels, Layered nanomaterials- a review, Glob. J. Eng. Des. Technol. 1 (2012) 32–41, http://www.gifre.org/admin/papers/gjedt/1222-32-41.pdf, http://www.gifre.org/admin/papers/gjedt/1222-32-41.pdf.

[45] J. Serafin, M. Baca, M. Biegun, E. Mijowska, R.J. Kaleńczuk, J. Sreńsek-Nazzal, B. Michalkiewicz, Direct conversion of biomass to nanoporous activated biocarbons for high CO2 adsorption and supercapacitor applications, Appl. Surf. Sci. 497 (2019), 143722, https://doi.org/10.1016/j.apsusc.2019.143722.

[46] E. Taer, A. Apriwandi, M.A. Mardiah, A. Awitdrus, R. Taslim, Synthesis free-template highly micro-mesoporous carbon nanosheet as electrode materials for boosting supercapacitor performances, Int. J. Energy Res. 46 (2022) 18740–18756, https://doi.org/10.1002/er.8493.

[47] J. Wang, Y. Xu, M. Yan, B. Ren, X. Dong, J. Miao, L. Zhang, X. Zhao, Z. Liu, Preparation and application of biomass-based porous carbon with S, N, Zn, and Fe heteroatoms loading for use in supercapacitors, Biomass Bioenergy 156 (2022), 106301, https://doi.org/10.1016/j.biombioe.2021.106301.

[48] E. Wahyuni, E. Taer, A. Sulistyo, R. Taslim, Cassava peel derived self-doped and hierarchical porous carbon as an optimized electrode for the ultra-high energy density of supercapacitor, Diam. Relat. Mater. 129 (2022), 109407, https://doi.org/10.1016/j.diamond.2022.109407.

[49] Q. Wu, M. Gao, C. Jiang, X. Gu, Z. Wang, L. Huang, Carbon-carbon dense network composite with hierarchical structure for additive-free and high volumetric performance supercapacitor, J. Power Sources 497 (2021), 229878, https://doi.org/10.1016/j.jpowsour.2021.229878.

[50] E. Taer, Y. Susanti, A. Awitdrus, S. Sugianto, R. Taslim, R.N. Setiadi, S. Bahri, A. Agustino, P. Dewi, B. Kurniasih, The effect of CO2 activation temperature on the physical and electrochemical properties of activated carbon monolith from banana stem waste, AIP Conf. Proc. 1927 (2018) 030016-1–030016-5, https://doi.org/10.1063/1.5021209.

[51] E. Taer, A. Apriwandi, R. Taslim, A. Agutino, D.A. Yusra, Conversion Syzygium oleana leaves biomass waste to porous activated carbon nanosheet for boosting supercapacitor performances, J. Mater. Res. Technol. 9 (2020) 13332–13340, https://doi.org/10.1016/j.jmrt.2020.09.049.

[52] A. Sarwar, M. Ali, A.H. Khoja, A. Nawar, A. Waqas, R. Liaquat, S.R. Naqvi, M. Asjid, Synthesis and characterization of biomass-derived surface-modified activated carbon for enhanced CO2 adsorption, J. CO2 Util. 46 (2021) 101476, https://doi.org/10.1016/j.jcou.2021.101476.

[53] A.K. Samanta, G. Basu, L. Mishra, Role of major constituents of coconut fibres on absorption of ionic dyes, Ind. Crop. Prod. 117 (2018) 20–27, https://doi.org/10.1016/j.indcrop.2018.02.080.

[54] S. Ahmed, M. Parvaz, R. Johari, M. Rafat, Studies on activated carbon derived from neem (Azadirachta indica) bio-waste, and its application as supercapacitor electrode, Mater. Res. Express 5 (2018), 045601, https://doi.org/10.1088/2053-1591/aab924.

[55] H. Chen, H. Wei, N. Fu, W. Qian, Y. Liu, H. Lin, S. Han, Nitrogen-doped porous carbon using ZnCl2 as activating agent for high-performance supercapacitor electrode materials, J. Mater. Sci. 53 (2018) 2669–2684, https://doi.org/10.1007/s10853-017-1453-3.

[56] E. Taer, F. Febriyanti, W.S. Mustika, R. Taslim, A. Agustino, A. Apriwandi, Enhancing the performance of supercapacitor electrode from chemical activation of carbon nanofibers derived Areca catechu husk via one-stage integrated pyrolysis, Carbon Lett. (2020), https://doi.org/10.1007/s42823-020-00191-5.

[57] S. Bai, C. Fan, L. Li, X. Wu, Synthesis of two-dimensional porous carbon nanosheets for high performance supercapacitors, J. Electroanal. Chem. 886 (2021), 115119, https://doi.org/10.1016/j.jelechem.2021.115119.

[58] Y. Wang, M. Qiao, X. Mamat, Nitrogen-doped macro-meso-micro hierarchical ordered porous carbon derived from ZIF-8 for boosting supercapacitor performance, Appl. Surf. Sci. 540 (2021), 148352, https://doi.org/10.1016/j.apsusc.2020.148352.

[59] M. Chen, D. Yu, X. Zheng, X. Dong, Biomass based N-doped hierarchical porous carbon nanosheets for all-solid-state supercapacitors, J. Energy Storage 21 (2019) 105–112, https://doi.org/10.1016/j.est.2018.11.017.

[60] T. Li, R. Ma, X. Xu, S. Sun, J. Lin, Microwave-induced preparation of porous graphene nanosheets derived from biomass for supercapacitors, Microporous Mesoporous Mater. 324 (2021), 111277, https://doi.org/10.1016/j.micromeso.2021.111277.

[61] G. Zhang, T. Guan, M. Cheng, Y. Wang, N. Xu, J. Qiao, F. Xu, Y. Wang, J. Wang, K. Li, Harvesting honeycomb-like carbon nanosheets with tunable mesopores from mild-modified coal tar pitch for high-performance flexible all-solid-state supercapacitors, J. Power Sources 448 (2020), 227446, https://doi.org/10.1016/j.jpowsour.2019.227446.

[62] B.S. Girgis, Y.M. Temerk, M.M. Gadelrab, I.D. Abdullah, X-ray diffraction patterns of activated carbons prepared under various conditions, Carbon Sci. 8 (2007) 95–100, https://doi.org/10.5714/cl.2007.8.2.095.

[63] C.K. Roy, S.S. Shah, A.H. Reaz, S. Sultana, A.N. Chowdhury, S.H. Firoz, M.H. Zahir, M.A. Ahmed Qasem, M.A. Aziz, Preparation of hierarchical porous activated carbon from Banana leaves for high-performance supercapacitor: effect of type of electrolytes on performance, Chem.Asian J. 16 (2021) 296–308, https://doi.org/10.1002/asia.202001342.

[64] E. Taer, L. Pratiwi, Apriwandi, W.S. Mustika, R. Taslim, Agustino, Three-dimensional pore structure of activated carbon monolithic derived from hierarchically bamboo stem for supercapacitor application, Commun. Sci. Technol. 5 (2020) 22–30, https://doi.org/10.21924/cst.5.1.2020.180.

[65] J. Sodtipinta, T. Amornsakchai, P. Pakawatpanurut, Nanoporous carbon derived from agro-waste pineapple leaves for supercapacitor electrode, Adv. Nat. Sci. Nanosci. Nanotechnol. 8 (2017), 035017, https://doi.org/10.1088/2043-6254/aa7233.

[66] C. Ding, T. Liu, X. Yan, L. Huang, S. Ryu, J. Lan, Y. Yu, W.H. Zhong, X. Yang, AN ultra-microporous carbon material boosting integrated capacitance for cellulose-based supercapacitors, Nano-Micro Lett. 12 (2020) 63, https://doi.org/10.1007/s40820-020-0393-7.

[67] B. Dinesh, K.S. Shalini Devi, A.S. Kumar, Curcumin-quinone immobilised carbon black modified electrode prepared by in-situ electrochemical oxidation of curcumin-phytonutrient for mediated oxidation and flow injection analysis of sulfide, J. Electroanal. Chem. 804 (2017) 116–127, https://doi.org/10.1016/j.jelechem.2017.09.054.

[68] K. Kumar, R.K. Saxena, R. Kothari, D.K. Suri, N.K. Kaushik, J.N. Bohra, Correlation between adsorption and X-ray diffraction studies on viscose rayon based activated carbon cloth, Carbon 35 (1997) 1842–1844, https://doi.org/10.1016/S0008-6223(97)87258-2. N. Y.

[69] M. Deraman, R. Daik, S. Soltaninejad, N.S.M. Nor, Awitdrus, R. Farma, N.F. Mamat, N.H. Basri, M.A.R. Othman, A new empirical equation for estimating specific surface area of supercapacitor carbon electrode from X-ray diffraction, Adv. Mater. Res. 1108 (2015) 1–7, https://doi.org/10.4028/www.scientific.net/AMR.1108.1.

[70] A. Gopalakrishnan, S. Badhulika, From onion skin waste to multi-heteroatom self-doped highly wrinkled porous carbon nanosheets for high-performance supercapacitor device, J. Energy Storage 38 (2021), 102533, https://doi.org/10.1016/j.est.2021.102533.

[71] H. Yang, J. Zhou, M. Wang, S. Wu, W. Yang, H. Wang, From basil seed to flexible supercapacitors: green synthesis of heteroatom-enriched porous carbon by self-gelation strategy, Int. J. Energy Res. 44 (2020) 4449–4463, https://doi.org/10.1002/er.5222.

[72] Z. Shang, X. An, L. Liu, J. Yang, W. Zhang, H. Dai, H. Cao, Q. Xu, H. Liu, Y. Ni, Chitin nanofibers as versatile bio-templates of zeolitic imidazolate frameworks for N-doped hierarchically porous carbon electrodes for supercapacitor, Carbohydr. Polym. 251 (2021), 117107, https://doi.org/10.1016/j.carbpol.2020.117107.

[73] S.X. Liang, F.F. Duan, Q.F. Lü, H. Yang, Hierarchical biocarbons with controlled micropores and mesopores derived from kapok fruit peels for high-performance supercapacitor electrodes, ACS Omega 4 (2019) 5991–5999, https://doi.org/10.1021/acsomega.9b00148.

[74] Q. Zhang, K. Han, S. Li, M. Li, J. Li, K. Ren, Synthesis of garlic skin-derived 3D hierarchical porous carbon for high-performance supercapacitors, Nanoscale 10 (2018) 2427–2437, https://doi.org/10.1039/c7nr07158b.

[75] M.Z. Iqbal, S. Zakar, S.S. Haider, Role of aqueous electrolytes on the performance of electrochemical energy storage device, J. Electroanal. Chem. 858 (2020), 113793, https://doi.org/10.1016/j.jelechem.2019.113793.

[76] E. Taer, R. Taslim, A. Apriwandi, Biomass-based self-single-oxygen heteroatom doped hierarchical porous carbon nanosheet for high-performance symmetrical supercapacitor, ChemNanoMat 8 (2022), e202200217, https://doi.org/10.1002/cnma.202200217.

[77] G.A. Yakaboylu, T. Yumak, C. Jiang, J.W. Zondlo, J. Wang, E.M. Sabolsky, Preparation of highly porous carbon through slow oxidative torrefaction, pyrolysis, and chemical activation of lignocellulosic biomass for high-performance

supercapacitors, EnergyFuels 33 (2019) 9309–9329, https://doi.org/10.1021/acs.energyfuels.9b01260.

[78] Y. Wang, W. Li, L. Zhang, X. Zhang, B. Tan, J. Hao, X. Jian Zhang, Q. Wang, X. Lu. Hu, Amorphous cobalt hydrogen phosphate nanosheets with remarkable electrochemical performances as advanced electrode for supercapacitors, J. Power Sources 449 (2020), 227487, https://doi.org/10.1016/j.jpowsour.2019.227487.

[79] J. Zhou, L. Hou, S. Luan, J. Zhu, H. Gou, D. Wang, F. Gao, Nitrogen codoped unique carbon with 0.4 nm ultra-micropores for ultrahigh areal capacitance supercapacitors, Small 14 (2018) 1–9, https://doi.org/10.1002/smll.201801897.

[80] T. Liu, J. Liu, L. Zhang, B. Cheng, J. Yu, Construction of nickel cobalt sulfide nanosheet arrays on carbon cloth for performance-enhanced supercapacitor, J. Mater. Sci. Technol. 47 (2020) 113–121, https://doi.org/10.1016/j.jmst.2019.12.027.

[81] G.A. Yakaboylu, C. Jiang, T. Yumak, J.W. Zondlo, J. Wang, E.M. Sabolsky, Engineered hierarchical porous carbons for supercapacitor applications through chemical pretreatment and activation of biomass precursors, Renew. Energy 163 (2021) 276–287, https://doi.org/10.1016/j.renene.2020.08.092.

[82] J. Mi, X.R. Wang, R.J. Fan, W.H. Qu, W.C. Li, Coconut-shell-based porous carbons with a tunable micro/mesopore ratio for high-performance supercapacitors, EnergyFuels 26 (2012) 5321–5329, https://doi.org/10.1021/ef3009234.

[83] N.H. Basri, M. Deraman, S. Kanwal, I.A. Talib, J.G. Manjunatha, A.A. Aziz, R. Farma, Supercapacitors using binderless composite monolith electrodes from carbon nanotubes and pre-carbonized biomass residues, Biomass Bioenergy 59 (2013) 370–379, https://doi.org/10.1016/j.biombioe.2013.08.035.

[84] Atika, R.K. Dutta, Oxygen-rich porous activated carbon from eucalyptus wood as an efficient supercapacitor electrode, Energy Technol. 9 (2021) 1–12, https://doi.org/10.1002/ente.202100463.

[85] W. Li, C. Chen, H. Wang, P. Li, X. Jiang, J. Yang, J. Liu, Hierarchical porous carbon induced by inherent structure of eggplant as sustainable electrode material for high

performance supercapacitor, J. Mater. Res. Technol. 17 (2022) 1540–1552, https://doi.org/10.1016/j.jmrt.2022.01.056.

[86] L. Zheng, X. Dai, Y. Ouyang, Y. Chen, X. Wang, Highly N/O co-doped carbon nanospheres for symmetric supercapacitors application with high specific energy, J. Energy Storage 33 (2021), 102152, https://doi.org/10.1016/j.est.2020.102152.

[87] Y. Qiao, R. Zhang, R. Li, W. Fang, Z. Cui, D. Zhang, Green synthesis of hierarchical porous carbon with adjustable porosity for high performance supercapacitors, Diam. Relat. Mater. 117 (2021), 108488, https://doi.org/10.1016/j.diamond.2021.108488.

[88] C. Wang, D. Wu, H. Wang, Z. Gao, F. Xu, K. Jiang, A green and scalable route to yield porous carbon sheets from biomass for supercapacitors with high capacity, J. Mater. Chem. A 6 (2018) 1244–1254, https://doi.org/10.1039/c7ta07579k.

[89] B. Liu, M. Yang, D. Yang, H. Chen, H. Li, Medulla tetrapanacis-derived O/N co-doped porous carbon materials for efficient oxygen reduction electrocatalysts and high-rate supercapacitors, Electrochim. Acta 272 (2018) 88–96, https://doi.org/10.1016/j.electacta.2018.04.001.

[90] T. Mitravinda, S. Anandan, C.S. Sharma, T.N. Rao, Design and development of honeycomb structured nitrogen-rich cork derived nanoporous activated carbon for high-performance supercapacitors, J. Energy Storage 34 (2021), 102017.

[91] S. Saha, D. Potphode, C.S. Sharma, Borassus flabellifer fruit flesh derived hierarchical porous partly graphitic carbon as a sustainable electrode for supercapacitors, EnergyFuels 36 (2022) 638–654, https://doi.org/10.1021/acs.energyfuels.1c03235.

[92] D. Potphode, S. Saha, C.S. Sharma, Carbon nanosheets decorated activated carbon derived from borassus flabellifer fruit skin for high performance supercapacitors, J. Electrochem. Soc. 167 (2020), 140508, https://doi.org/10.1149/1945-7111/abbfdb.